UNIVERSITY OF JYVÄSKYLÄ
DEPARTMENT OF CHEMISTRY
RESEARCH REPORT No. 122

THEORETICAL STUDIES OF ATOMIC SCALE IMPURITIES IN SUPERFLUID ^{4}He

BY

LAURI LEHTOVAARA

Academic Dissertation
for the Degree of
Doctor of Philosophy

Jyväskylä, Finland
2007

DEPARTMENT OF CHEMISTRY, UNIVERSITY OF JYVÄSKYLÄ
RESEARCH REPORT No. 122

THEORETICAL STUDIES OF ATOMIC SCALE IMPURITIES IN SUPERFLUID ^{4}He

BY

LAURI LEHTOVAARA

Academic Dissertation
for the Degree of
Doctor of Philosophy

To be presented, by permission of the Faculty of Mathematics and Natural Sciences of the University of Jyväskylä, for public examination in Auditorium FYS1, on 13th April 2007, at 12 noon.

University of Jyväskylä
Jyväskylä, Finland
ISBN 978-951-39-2779-0
ISSN 0357-346X

URN:ISBN:978-952-86-0491-4
ISBN 978-952-86-0491-4 (PDF)
ISSN 0357-346X

University of Jyväskylä, 2025

OPPONENT

Professor Martti Puska
Laboratory of Physics
Helsinki University of Technology

SUPERVISORS

Professor Henrik Kunttu
Department of Chemistry
University of Jyväskylä

Professor Jussi Eloranta
Department of Chemistry and Biochemistry
California State University at Northridge

REVIEWERS

Professor V. Ara Apkarian
Department of Chemistry
University of California, Irvine

Professor Jesus Navarro Faus
Instituto de Fisicia Corpuscular
University of Valencia

Preface

The work represented in this thesis was carried out between years 2002 and 2007 at the Department of Chemistry, University of Jyväskylä.

I've been priviledged to have extraordinary people around me. First of all, I wish to thank Professor Henrik Kunttu for “finding” me and believing in me, thus making it all possible. His support during the actual writing of the thesis was also crucial. I'm extremely grateful to my mentor Professor Jussi Eloranta for his patience, guidance, and encouragement. Many thanks goes to Dr. Toni Kiljunen for his help and patience, especially during the first years on my academic career, and to Dr. Jari Toivanen for his help in the field of numerical methods. I also wish to thank all the fellow physico-chemists for the pleasant working environment, which they have provided. Special thanks goes to Dr. Jussi Ahokas for his ability to work as a mental safety valve.

The financial support from the Ministry of Education, the Graduate School of Computational Chemistry and Molecular Spectroscopy, and University of Jyväskylä, as well as the computational resources from the Center of Scientific Computing, are gratefully acknowledged. I would like to thank Professor Emeritus Matti Nurmia for revising the language of this thesis.

Finally, I express my deepest gratitude to Katri, to my family, and to my friends. Without you I would have lost my mind.

Jyväskylä, April 2007
Lauri Lehtovaara

Abstract

The macroscopic properties of superfluid helium are well known and their microscopic background is understood to a good extent. However, the microscopic description of superfluid in the presence of atomic scale anisotropy, for example, an atom or a molecule, is not complete and it has been extensively studied in the recent years. Especially, the dynamic properties have remained as a challenge.

The earlier theoretical studies on atomic scale impurities in superfluid ^{4}He have mainly used the standard (classical) bubble model, the quantum Monte Carlo methods, or the one-dimensional density functional theory, all of which having their own specific restrictions. In the present thesis, a fully three-dimensional bosonic density functional method is developed, which enables the study of a variety of time-dependent and time-independent, anisotropic systems. Fully three-dimensional systems are computationally very demanding and an efficient numerical implementation is crucial. Thus a lot of attention must be paid to the design of the implementation.

The developed method was applied to three different systems: 1) molecular hydrogen solvated in bulk superfluid helium, 2) a hypothetical two-level atom in a helium droplet, and 3) electron bubbles in bulk superfluid. The solvation of the first four triplet states of H_2 was studied using the bosonic density functional method and a hybrid density functional – diffusion Monte Carlo method. The solvation structures as well as absorption and emission spectra were calculated. The absorption spectrum of a hypothetical two-level atom, which is excited from its anisotropic (isotropic) ground state to its isotropic (anisotropic) excited state, was simulated by recording the time evolution of the system. The absorption spectra obtained are compared with the corresponding isotropic cases and the spectra were found essentially equal in small helium droplets. Electron bubbles in superfluid ^{4}He were calculated using a combination of electronic and bosonic density functional methods. As a result, the properties of the first three states of one-electron bubbles were obtained and the two-electron bubble was found unstable in its both (singlet and triplet) states.

Original publications

This thesis is based on the following original research papers:

I **Solvation of triplet Rydberg states of molecular hydrogen in superfluid helium**
Toni Kiljunen, Lauri Lehtovaara, Henrik Kunttu, and Jussi Eloranta
Physical Review A, **69**, 012506 (2004)
https://doi.org/10.1103/PhysRevA.**69**.01250**6**

II **Efficient numerical method for simulating static and dynamic properties of superfluid helium**
Lauri Lehtovaara, Toni Kiljunen, and Jussi Eloranta
Journal of Computational Physics, **194**, 78–91 (2004)
https://doi.org/10.101**6**/j.jcp.2003.08.020

III **A 2-level anisotropic electronic system in superfluid ^{4}He**
Lauri Lehtovaara and Jussi Eloranta
Journal of Low Temperature Physics, **138** 91–96 (2005)
https://doi.org/10.1007/s10**9**0**9**–005–1533–7

IV **Solution of time-independent Schrödinger equation by the imaginary time propagation method**
Lauri Lehtovaara, Jari Toivanen, and Jussi Eloranta
Journal of Computational Physics, **221**, 148–157 (2007)
https://doi.org/10.101**6**/j.jcp.200**6**.0**6**.00**6**

V **One and two-electron bubbles in superfluid ^{4}He**
Lauri Lehtovaara and Jussi Eloranta
Journal of Low Temperature Physics, in press (2007)
https://doi.org/10.1007/s10909-007-9348-3

The author of this thesis has contributed in writing papers I–V. In the papers II, IV and V, the author has also participated in developing the theory. In the paper I, the author has performed the variational and diffusion Monte Carlo calculations, the 3D bosonic density functional calculations, and the numerical solution of the vibrational wavefunctions. The calculations were done using computer programs developed by the author. In papers II-V, the author has perfomed all calculations using programs developed by himself.

Other publications

Other publications, which are not included but related to this thesis, are listed below:

VII **Small multielectron bubbles in bulk superfluid ^{4}He**
Lauri Lehtovaara and Jussi Eloranta
AIP Conference Proceedings, **850**, 167 (2006)

VIII **Applicability of density functional theory to model molecular solvation in superfluid ^{4}He**
Teemu T. Isojärvi, Lauri Lehtovaara and Jussi Eloranta
AIP Conference Proceedings, **850**, 386 (2006)

Contents

Chapter 1

Introduction

Since its discovery in 1938 by P.L. Kapitza [1, 2] superfluid helium has been extensively studied. Early experiments were focused on the macroscopic properties of superfluid helium revealing its extraordinary properties, such as vanishing viscosity. Theoretical studies made by famous scientists, such as L.D. Landau [3] and R.D. Feynman [4 8], formed the basis for understanding the underlying physics of superfluidity. More recent experiments have been more focused on atomic scale phenomena, for example, the static and dynamic properties of superfluid helium around atomic scale impurities. To explain the observations made in these experiments, new theoretical and numerical methods have been developed. The present thesis focuses on these developments.

1.1 Superfluid ^{4}He

A helium atom consists of a nucleus and an electron pair, which fills the $1s$ atomic orbital. The electrons are strongly bound as the first excited state lies $\sim$20 eV above the ground state [9]. As a result the chemical interactions between a helium atom and other atoms or molecules are very weak and no stable molecules containing a helium atom are known. The van der Waals' forces (induced dipole – induced dipole interaction) are also weak because helium atoms are weakly polarizable. The light mass of helium atoms contributes to a large zero point energy. For example, He–He pair-interaction is only about 1 meV bound, and consequently the dimer has an equilibrium distance of the order of nanometers [10–12]. Illustratively, to other atoms, a helium atom looks like a small, light, hard ball, which attracts slightly at close distances, but strongly prevents penetration inside the ball.

Of the two stable isotopes, ^{3}He and ^{4}He, ^{4}He is the more common (>99.99%) in nature. It has two protons and two neutrons in its nucleus with both nuclear spins paired. Together with the paired electron spins it is a boson with a total spin equal to zero. This light, inert boson has a very exceptional phase diagram as shown in Figure 1.1. In addition to the gas, liquid and solid forms it possesses a superfluid phase. When liquid helium is cooled at the saturated vapor pressure, it undergoes a phase transition at the λ-point (2.17 K) [13]. A fraction of the liquid begins to behave purely quantum mechanically and remains liquid down to absolute zero. To describe the macroscopic properties of the superfluid phase (He-II), the two-fluid model can be used [3,14]. In this model the superfluid phase is assumed to consist of two different fluids: a "pure" superfluid and a normal fluid. The contribution of the superfluid fraction increases as the temperature is decreased below the λ-point and reaches unity at 0 K (Figure 1.2).

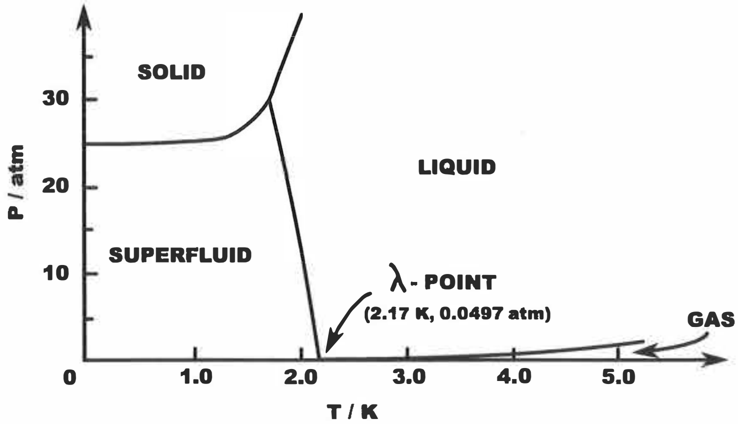

Figure 1.1: Phase diagram of ^{4}He. The four different phases are shown: the gas, liquid, solid, and superfluid. Reproduced from reference [13].

1.1.1 Macroscopic view

On the macroscopic scale, the superfluid has several unusual properties compared to a normal fluid; they are briefly reviewed in this subsection using the two-fluid picture. A more detailed and correct description is presented in the next subsection, which provides the description on the microscopic level. A pure superfluid has no viscosity, which allows it to pass through

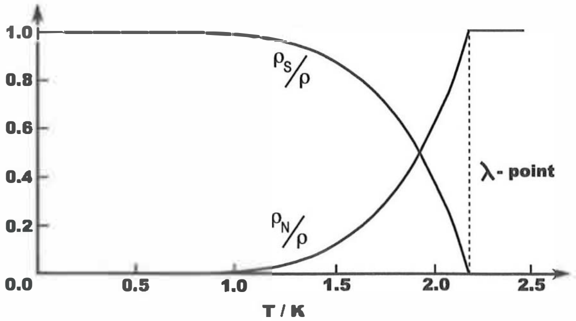

Figure 1.2: Superfluid (ρ_s/ρ) and normal fluid fractions (ρ_n/ρ). Reproduced from reference [13].

tiny holes and capillaries without any friction, *i.e.*, without dissipating energy [13]. It has zero entropy and infinite thermal conductivity [13], which means that the superfluid fraction is always at zero temperature, whereas, at finite temperatures, the normal fraction contains all the heat of the system. This allows, for example, temperature waves (the second sound), which are able to transfer heat without altering the total density [13].

In the thermomechanical effect a superfluid flow is created by heating a capillary inserted in liquid helium [13]. The diameter of the capillary is so small that only the superfluid fraction can flow through it. When the capillary is heated, the amount of normal fraction increases inside the capillary. As a consequence, the imbalance between the liquid inside the capillary and the surrounding liquid causes a flow of the superfluid into the heated capillary. Continuous heating creates a continuous flow and the superfluid fraction flows through the capillary. As a result the heated capillary acts as a thermomechanical pump (Figure 1.3), which is also known as the fountain pump.

Vortices are visible evidence of the underlying quantum nature of the superfluid. When a superfluid is rotated faster than a given critical velocity, a vortex may form with a certain minimum angular velocity. If the rotation speed is increased, the angular velocity of the vortex remains constant, until another vortex appears. Although the angular velocity of the first vortex may change, the circulation ("amount of rotation") remains unchanged and the new vortex has the same circulation as the first one. By increasing rotation even further, more vortices with the same circulation are introduced. This behaviour is explained by the superfluid's quantum nature. The superfluid acts as a single quantum mechanical entity and a rotating superfluid can only accommodate energy in amounts equal to the size of a vortex circulation

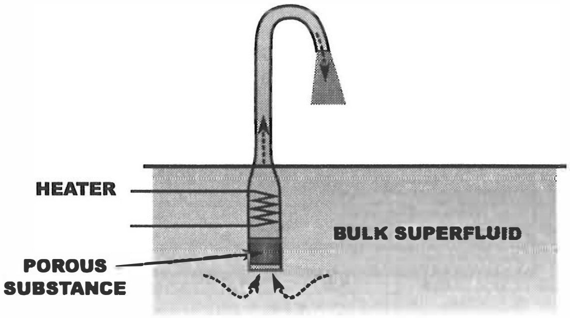

Figure 1.3: Thermomechanical pump for superfluid ^{4}He known as the fountain pump. Reproduced from reference [13].

quantum [13].

1.1.2 Microscopic view

In order to properly explain the macroscopic properties of superfluid helium, one must examine the quantum mechanics of the system. The superfluid phase is a Bose–Einstein condensate, which can be considered as composed of two fractions [4, 15]. The part of the system which is in the ground state corresponds to the superfluid (condensate) fraction, and the excited states are represented as the normal fraction of the two-fluid model. As the helium atoms are bosons, the total wavefunction of the system must be symmetric and atoms cannot be distinguished from each other. Therefore, every atom contributes to both superfluid and normal fluid, and no phase separation exists. The Bose–Einstein condensation happens despite the strong repulsive interaction at short distances, since "the motion of one atom through the others is not opposed by a potential barrier, because the others may move out of the way" [4]. The motion in the configuration space happens along trajectories of low kinetic energy and negligible potential barriers. In other words, the zero point motion of the atoms ($\oslash$ 2.7Å) is sufficient to keep the atoms far enough (~3.6Å) from each other so that the atoms can move easily past each other [5]. Illustratively, the hard balls must be able to pass each other without colliding and without a major readjustment of the other balls. The motion of the other atoms just increases the effective inertia of the moving atom. The atoms delocalize, which allows for condensation, and thus the ground state wavefunction spans over the whole liquid. The corresponding density is uniform throughout the system, but it has zero-point fluctuations analogous to the vacuum electromagnetic field, with the exception that only longitudinal modes are allowed [5].

The elementary excitations of superfluid helium are the key to understanding the two-fluid model. The excitations are divided into two types: phonons and rotons. The phonons are long wavelength compressional waves, *i.e.*, sound waves, where each atom is slightly displaced to form a periodic, long wavelength modulation in the density (Figure 1.4a). Phonons exist in normal fluids, whereas rotons do not. According to Feynman "the roton is a kind of quantum-mechanical analog of a microscopic vortex ring, of diameter about equal to the atomic spacing" [6] (Figure 1.4b), which is completely delocalized. In contrast to the behavior of a phonon, a roton leaves the density unchanged in scales larger than the interatomic distance. However, it needs a finite energy to be excited, whereas the energy of a phonon is proportional to the square of the momentum, and thus the energy approaches zero as the wavelength approaches infinity [5]. The phonons and rotons are the only possible (elementary) excitations that can be thermally created. Because of the finite excitation energy of the rotons, there is not enough thermal energy for the creation of appreciably many rotons just above the absolute zero (below ~1 K) [5].

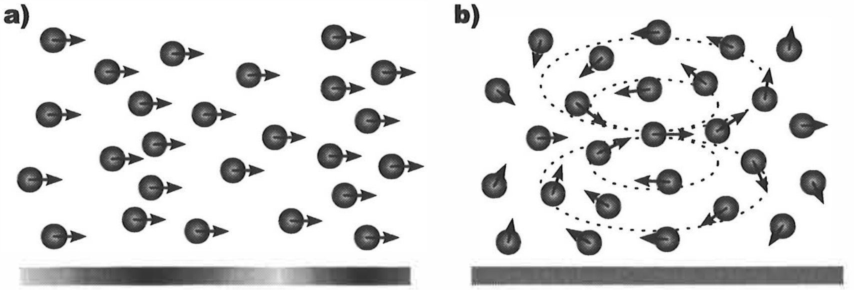

Figure 1.4: Illustrative sketch of a) a phonon and b) a roton wave packet. Arrows, current; greyscale bar, density.

Before considering the theory of superfluidity in detail, a few remarks should be made regarding the peculiar excitation spectrum, the dispersion relation. The spectrum of the elementary excitations (Figure 1.5) can be derived from data obtained in the inelastic neutron scattering experiments [16]. Initially, the energy rises linearly in the region that corresponds to phonons. The rotons are found near momentum $q = 2$ Å^{-1}, where the dispersion relation has its minimum, called the roton minimum. Note that at the roton minimum and at the maximum of the spectrum, called the maxon, the group velocity is equal to zero, *i.e.*, a wave packet at these points does not move even though it has a non-zero momentum. Between the maxon and the roton minimum, the group velocity is negative, *i.e.*, a wave packet moves to the opposite direction relative to the momentum.

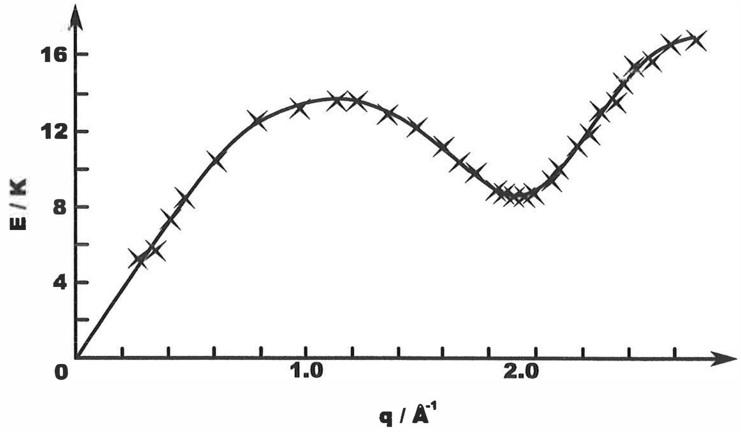

Figure 1.5: Dispersion relation of bulk superfluid ^{4}He. Reproduced from reference [13].

One manifestation of superfluidity is observed when an object is dragged slowly in the superfluid: it drifts without friction [13]. In the microscopic view, an object moving through the liquid can only feel friction if it can dissipate energy [5]. The only way to dissipate energy in superfluid is to create excitations in the liquid. However, the conservation of energy and momentum prevents an object moving with a constant velocity from creating phonons and rotons when its velocity is below a certain critical velocity [5]. The critical velocity of phonons is the velocity of the (first) sound, 239 m/s, whereas for the rotons the critical velocity is significantly lower, ~59 m/s [13]. Therefore, below the critical velocity (of the rotons), if no excitations are present, *i.e.*, the temperature is zero, the object does not have any way to lose its energy and thus it cannot feel any friction [5]. However, at a finite temperature, there exist thermal excitations (*e.g.* phonons and rotons), which can scatter from the object and cause it to lose some of its energy [5]. This energy loss can be arbitrarily small. Illustratively, the object can be regarded as moving in a gas of thermal excitations with non-zero viscosity, which corresponds to the normal fluid in the two-fluid model.

Another consequence of superfluidity is a superfluid flow through a capillary. In this case, the thermal excitations are not able to work their way through the long, narrow capillary [5], because the modes of the bulk are weakly coupled to the modes in the capillary, and thus the excitations are mainly reflected back. However, because the ground state wavefunction just adapts to the shape of the capillary while remaining essentially unchanged in other respects, the coupling is strong for the superfluid fraction. As the superfluid fraction can flow through the capillary, whereas the normal fraction cannot, only a superfluid flow is observed.

If the temperature at one end of the capillary is higher than at the other end, the average amount and the average momentum of thermal phonons are greater at the hotter end than at the colder end. This causes a higher pressure at the hotter end, as the pressure is created by phonons colliding with the walls of a container [5]. This pressure difference causes a superfluid flow from the hot to the cold end, which is the explanation for the thermomechanical effect.

Finally, the quantum mechanics of vortices are briefly described. A vortex is a circulation of the fluid around a line inside the superfluid. The wavefunction of the superfluid wraps around the line in such a way that the phase changes by a non-zero integer multiple of 2π in one cycle around the line. The multiplier, *i.e.*, the quantum number of the vortex, must be an integer to satisfy the continuity requirement of the wavefunction, and non-zero to yield the circulation. The circulation of a (simply connected) superfluid with a uniform density is prevented by the Bose statistic, as the circulation reduces to the permutation of atoms [6]. Thus, the minimum energy solution for circulating superfluid is obtained when the density vanishes on the vortex line (and superfluid becomes multiply connected) [8]. The superfluid can circulate around the vortex line with a constant angular velocity, as the divergence of the kinetic energy in the core is canceled by the vanishing density. In the classical picture, the centrifugal forces are pushing the atoms out of the core.

A vortex line cannot have a loose end inside the liquid due to continuity, but it can terminate on the walls of the container, on impurities, or it can form a loop (Figure 1.6). A vortex ring can form if a vortex line, or a part of it, creates a closed loop and the loop detaches from a wall, from an impurity, or from the rest of the vortex line. This offers a novel way to create excitations in the superfluid. The energy of a vortex ring E_v is approximately proportional to radius of the vortex ring R ($E_v \propto R \ln \frac{R}{a}$) and is greater than the energy of a phonon or a roton [8]. A vortex ring also carries higher momentum, which is proportional to the area of the ring ($\propto R^2$) [8]. Thus a large vortex can absorb more momentum relative to its energy than a small one, and as large objects (*e.g.* impurity or capillary) can create large vortices, they have lower critical velocities than small objects. Because the conservation of energy and momentum is more easily satisfied by a vortex than a phonon or a roton, the vortices have lower critical velocities than phonons and rotons. In some sense, the roton can be regarded as the smallest possible vortex with a radius of the order of the atomic spacing [8].

As discussed earlier, when a superfluid is rotated, an array of vortices is observed. In an equilibrium, the number of vortices depends on the rotation speed and each of the vortices has the same minimum circulation corresponding to one circulation quantum. The array of small vortices allows a more favourable velocity distribution than, for example, one large vortex in a highly excited state, and the total energy is lower despite the increased number of holes in the liquid [8].

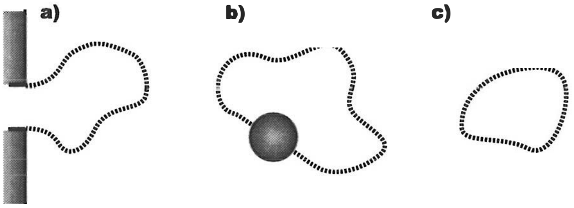

Figure 1.6: Sketches of different kind of vortices: a) a vortex line attached to a wall, b) a vortex line attached to an impurity atom, and c) a vortex ring.

1.2 Atomic scale impurities

The present understanding of the microscopic properties of superfluid helium is mainly based on inelastic neutron scattering experiments [16], which provide information about correlations in the liquid. However, these experiments probe only the homogeneous bulk liquid. As the presence of atomic scale impurities introduces microscopic inhomogeneities in the liquid, they can provide information on the microscopic properties of the inhomogeneous superfluid. In addition to being microscopic probes in the superfluid, the impurities themselves can be studied in great detail, as the superfluid offers a homogeneous, ultra-cold and gentle matrix for spectroscopic studies [17].

The major obstacle in introducing impurities into bulk superfluid helium is the very low equilibrium solubility and rapid clustering of the atoms and molecules. This is why the first studies were carried out using intrinsic impurities, such as helium ions (He^+), excited helium atoms (He^*) and molecules (He_2^*), and excess electrons [17], which will be discussed in more detail later. In more recent experiments metal atoms and small metal clusters have been successfully introduced into superfluid by 1) first dragging ions into the liquid by an electric field and then neutralizing them or 2) by pulsed laser ablation of a metal target either just above the helium surface or immersed in the helium [17]. Similar techniques have also been applied to hydrogen to obtain hydrogen molecules [18].

The development of the helium droplet technique has been the most successful in solving the problem of how to introduce chemical species into liquid helium, as virtually any atom or molecule can be picked up by a droplet (Figure 1.7) [17]. The droplets are created by expanding cold helium gas through a nozzle. As the gas expands, it cools down and, consequently, the atoms begin to cluster. After the clusters have grown to larger droplets, they are cooled further down to 0.4 K by evaporation of helium atoms. In a pickup cell, an impurity is captured by the droplet in a collision between the gaseous impurity atom and the droplet. The excess energy which remains after the collision quickly evaporates more helium atoms, and the droplet cools back to 0.4 K. Typical droplets used in the experiments consist of between 10^3 and 10^5 helium atoms. The droplets are sufficiently small and cold so that thermal phonons are not appreciably populated, and primarily only surfaces modes, ripplons, are thermally excited [19].

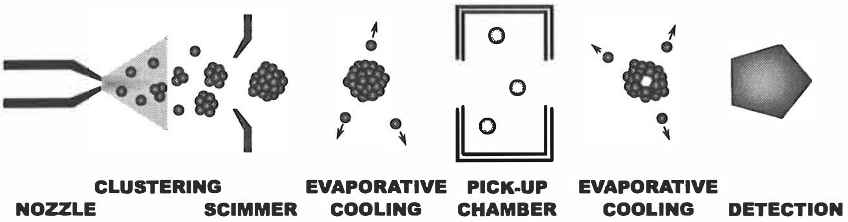

Figure 1.7: Schematic diagram of a helium droplet experiment.

In the experiments, different metals (*e.g.* Li, Na, K, Rb, Cs, Mg, Ca, Sr, Ag, Al) and their clusters, small molecules (*e.g.* SF_6, OCS, NH_3, HF) and organic molecules (*e.g.* glyoxal, polyaromatics, indoles, and porphyrines) have been studied in helium droplets [20]. Most of these are captured inside the droplet; however, for example, alkali metals attach to the surface of the droplet. To study optical spectra of these droplets two techniques are mainly used: the beam depletion technique and the laser-induced fluorescence method [17]. When an atom or molecule (chromophore) is excited by light, a rapid energy transfer from the chromophore to the surrounding liquid occurs and evaporation takes place, *i.e.*, the droplet is depleted. In the beam depletion approach, the depleted droplet is ionized and detected by a mass spectrometer. The laser-induced fluorescence method can provide a significantly better signal-to-noise ratio if the fluorescence quantum yield of the impurity is sufficiently high.

Impurities embedded in helium have a wide range of solvation structures from frozen solvent layers to large cavities. If the impurity–helium interaction is strongly repulsive, as in the case of an excess electron or a negative ion, a cavity ("bubble") is formed inside the liquid with the impurity residing at the center (Figure 1.8a) [17]. If the interaction is attractive, helium atoms are packed tightly around the impurity and solvation shells are formed (Figure 1.8b) [17]. The solvation shells remain in the liquid phase unless the attraction is large. In this case, some helium atoms might be "frozen" by forming a complex with the impurity [20].

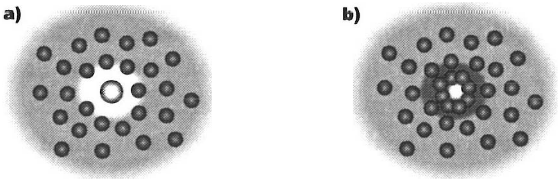

Figure 1.8: Illustrative view of an impurity a) "bubble", and b) "snowball". Greyscale background, helium density.

Electronic excitation of an impurity is coupled to the surrounding liquid. If this coupling is weak, the main feature shown in the spectrum is the zero phonon line (ZPL), which corresponds to the excitation of the (solvated) impurity alone. It is typically sharp and slightly shifted (~10–100 cm^{-1}) to blue or to red, depending on the helium–impurity interaction [20]. A simultaneous excitation of the impurity and helium yields a phonon wing on the blue side of the zero phonon line, *i.e.*, higher in the energy. A common feature of most phonon wings is a broad maximum around 8 K, which is considered as evidence of the superfluidity [20]. If the droplets are in the superfluid state, the density of states has a maximum at the roton minimum, at 8.65 K in the bulk and slightly less in droplets. Furthermore, if the transition probability is assumed to be smooth, the increased density of states produces a maximum at the corresponding energy. If the coupling between an impurity and helium is strong, as in the case of, for example, some aromatic molecules, it has been suggested that impurity–helium complexes or solid solvent layers are responsible for specific features below 8 K [20].

The vibrational bands in the IR-spectra of solvated impurities show only small changes with respect to the gas phase. The shifts are order of magnitude smaller ($\sim$1-10 cm^{-1}) than typical shifts of the electronic transitions [19, 20]. As no splitting of the degeneracies have been observed, it has been assumed that the superfluid does not affect the symmetry of the vibrations, *i.e.*, that the superfluid adapts to the symmetry of the molecule. A rotation structure is also observed for some molecules, which is not typical for liquid solvents [19]. Rotational constants of the light molecules, such as HF and H_2O, are equal to the gas phase values, whereas for slightly larger molecules, such as SF_6 and OCS, the rotation is somewhat hindered and the effective moment of inertia is increased approximately three-fold [19]. It has been proposed that the fraction of normal fluid is increased in the first solvation shell, which leads to a higher effective moment of inertia as normal fluid is dragged by the rotor [21].

Liquid helium offers an interesting opportunity to study chemical reactions at very low temperatures. In contrast to studies at higher temperatures, the reactions are not activated by thermal excitations, but instead the quantum mechanics, *e.g.*, tunneling, and long-range dipole–dipole (van der Waals') forces play an important role [20]. For example, the van der Waals' forces define how reactants approach each other, and thus dictate which reactions are likely to happen. This is in contrast to higher temperature conditions where the orientation of the reactants is thermally averaged. A selective recombination of alkali atoms to di- and trimers in liquid helium has been demonstrated [20]. Also a reaction between Ba and N_2O to form BaO^* and N_2, providing a strong chemiluminescence as BaO^* relaxes, has been studied [20]. In the future, helium droplets might be used as ultra cold nanoreactors.

Finally, a short comparison of the advantages and disadvantages between bulk and droplet experiments is made. As stated earlier, the droplets are superior in the sense that almost any species can be introduced in the droplets, whereas the advantages of the bulk are in the accessibility of a wide pressure and temperature range [17]. The droplet experiments may also suffer from unwanted boundary effects because of the microscopic size of the droplets. These two media are complementary to each other.

1.2.1 Electron bubbles

An excess electron in liquid helium deserves a more detailed inspection due to its extraordinary nature. Electrons can be introduced in helium by a discharge tip, or by an α or β–source immersed into helium, and they can then be dragged in a chosen direction by a static electric field for excitation and detection [22, 23]. In the early experiments, Levinc and Sanders noticed that the mobility of the excess electrons is decreased by a factor of 10^3 to 10^4 in liquid helium as compared to the gas phase [24]. This can be explained by the formation of an electron bubble in the liquid phase. In the gas phase, an excess electron is in a delocalized plane-wave state, but because the density increases, it localizes inside a cavity and its motion is hindered as the electron must "push" helium out of its way. The cavity is formed as the strong repulsion between the excess electron and electrons of helium favors the localization of the former, and the reduction in the potential energy is able to outweigh increase in the kinetic energy.

In its ground state, the electron bubble resembles an electron in a spherical square-well of a depth of ~1.0 eV. However, the spherical shape is a result of a delicate balance between the electron and the liquid. If the excess electron is excited to its first excited state, the wavefunction forms a nodal plane. As the electron density is no longer spherical, the liquid begins to adapt to the new shape. As a result, the shape of the bubble transforms from a sphere to a peanut (two slightly overlapping spheres). The strong coupling between the electron and helium leads to a unique bubble shape for each electronic state of the bubble in contrast to atoms or molecules, in which the nuclei dictate the shapes of the electronic wavefunctions.

Even though an excess electron was one of the first impurities inserted into liquid helium, some experimental observations still remain unexplained. Ihas and Sanders [22] measured the time–of flight for the electron bubbles in a static electric field and observed the so called "exotic ions" in addition to the electron bubbles in their ground state. The exotic ions were found to be faster than the ground state electron bubbles, which indicates either a smaller cross-section or a greater charge for the exotic ions. It has been suggested that the exotic ions could be, for example, excited one-electron bubbles or bubbles containing two electrons.

Chapter 2

Density functional theory

In the traditional wavefunction based quantum mechanics, one usually seeks for the lowest eigenvalue of the Hamiltonian operator and the corresponding multidimensional wavefunction with the proper symmetry: symmetric for bosons and antisymmetric for fermions. The dimension, *i.e.*, the degrees of freedom, of the wavefunction depends on the number of particles N in the system and, in a general case, it is three times the number of particles. If a system is composed of more than one particle, the Hamiltonian operator is a functional of the wavefunction, *i.e.*, the eigenvalue problem depends on its result. In principle, one must seek for a solution of a 3N–dimensional nonlinear eigenvalue problem, which is, in practice, impossible to solve, excluding a few special cases. Even after such approximations as the Hartree–Fock, one still has to solve a 3N–dimensional eigenvalue problem, which becomes increasingly difficult as the number of particles grows. Quickly, after the number of particles exceeds a few hundred or thousand, the solution is out of reach even for modern supercomputers. The main advantages of the wavefunction based approaches are that the Hamiltonian is exactly known and the results can be refined systematically.

The density functional theory is based on the fact that all physical observables of a system can be extracted from the density of the system. In other words, all physical observables are functionals of the density. As the density is a function of three variables, *e.g.*, the three spatial coordinates, instead of three variables per particle, it is much easier to work with the density than with the wavefunction as soon as the number of particles increases beyond a few. As the dimension of the problem does not, in principle, depend on the number of particles in a system, it makes the density functional theory especially suitable for large systems with many particles. The disadvantage of the density functional theory is that the exact forms for the functionals are not known and one must find reasonably good approximations for these, usually at least for the energy functional. Fortunately, sufficiently accurate approximations do exist for many systems.

2.1 Foundations of density functional theory

The first developments towards the density functional theory were made by Thomas [25] and Fermi [26,27], but the first proof that the density is sufficient to provide the ground state properties of a system was derived by Hohenberg and Kohn [28]. The proof was later refined by Levy [29]. In Levy's constrained search, one searches for the wavefunction which minimizes the total energy, excluding the external energy, for each possible density. The wavefunction is searched over all possible wavefunctions yielding the given density:

$$F[\rho] = \min_{\psi \to \rho} \langle \psi | \hat{T} + \hat{V}_{int} | \psi \rangle, \tag{2.1}$$

where $\hat{T}$ is the kinetic energy operator and $\hat{V}_{int}$ is the potential energy operator excluding the external potential. In the next stage, the external potential $v(\vec{r})$ is included and a search is made over all possible densities, which yield the correct number of particles, N:

$$E_0 = \min_{\rho \to N} \left[F[\rho] + \int v(\vec{r}) \rho(\vec{r}) d^3 r \right]. \tag{2.2}$$

This can be performed as the external potential depends only on the density and ignores any details of the wavefunction. The functional $F[\rho]$ is an universal functional of the density, *i.e.*, it depends *only* on the density and searches over *all possible* wavefunctions yielding the given density. Now, if the functional $F[\rho]$ is known, it is sufficient to search only over all densities instead of all wavefunctions. The problem is that the functional is not exactly known; however, many useful approximations have been developed, some of which are briefly reviewed later in this chapter.

In a way similar to Hohenberg's and Kohn's proof for time-independent problems, Runge and Gross [30] developed a proof for time-dependent problems. It proves by *reductio ad absurdum* that two time-dependent potentials $v(\vec{r}, t)$ and $v'(\vec{r}, t)$, which differ by more than a purely time-dependent function $c(t)$, cannot produce the same time-dependent density $\rho(\vec{r}, t)$ from the same initial density $\rho(\vec{r}, 0) = n_0(\vec{r})$. Later Kohl and Dreizler [31] introduced a proof which was based on a constrained search. They used the time-evolution operator of the system to propagate wavefunctions back in time and then utilized Levy's constrained search to find the wavefunction corresponding to the system's ground state. To sketch the proof, let us start with a density $\rho(\vec{r}, t)$ at time t, which has been propagating from the ground state density $\rho_0(\vec{r}) = \rho(\vec{r}, t = 0)$ under a time-dependent potential $v(\vec{r}, t)$. Because the time-dependent case has only a stationary condition for the action, but does not have a minimum condition, like the minimum energy principle of the time-independent case, the problem must be transformed to a time-independent problem in order to use the constrained search. This is done by applying the inverse of the system's time propagation operator to the set of all possible wavefunctions $\psi_\rho(\vec{r}, t)$, which yield the density $\rho(\vec{r}, t)$ at time t:

$$\psi_\rho(\vec{r}, 0) = \hat{U}^\dagger(t)\psi_\rho(\vec{r}, t), \tag{2.3}$$

where $U(t)$ is the time propagation operator from time zero to time t. Now, the wavefunction, which minimizes the energy at time zero, must be the ground state wavefunction and thus correspond to the density $\rho(\vec{r}, t)$ at time t. The density functional $K[\rho]$ searches this wavefunction:

$$K[\rho] = \min_{\psi(\vec{r},t) \to \rho(\vec{r},t)} \langle \psi(\vec{r}, t) | \hat{K}(t) | \psi(\vec{r}, t) \rangle \tag{2.4}$$

where

$$\hat{K}(t) = \hat{U}(t) \left[\hat{T} + \hat{V} + v(\vec{r}, t = 0) \right] \hat{U}^\dagger(t). \tag{2.5}$$

The functional $K[\rho]$ is not universal as it still depends on the system through the external potential $v(\vec{r}, t)$. However, time-dependent problems are initial value problems whereas time-independent problems are boundary value problems [32]. Therefore, the solution of a time-independent problem depends on the external potential, the number of particles, and the possible boundary conditions of the domain, whereas the time-dependent solution depends on the initial state and the external potential. Thus the density functionals for time-dependent systems are, in principle, bound to a fixed initial state. For example, the same molecule with different bond lengths might have different time-dependent density functionals. In practice, it is found that many approximations work well with a wide variety of different systems [32].

2.2 Electronic systems

Electronic systems are fermionic and require that the wavefunction is antisymmetric, *i.e.*, no two electrons can have exactly the same quantum state. This is why the constrained searches in the previous section should restrict the search to *antisymmetric* N–particle wavefunctions yielding the given density. The antisymmetry requirement makes it more difficult to design good approximations for functionals, especially for the kinetic energy. The basic scheme to overcome this problem is to use an approach developed by Kohn and Sham [33]. In this approach the total energy functional is divided to the kinetic energy, electron–electron interaction and external potential energy functionals:

$$E[\rho] = T[\rho] + V_{ee}[\rho] + \int v(\vec{r})\rho(\vec{r})\, d^3r. \tag{2.6}$$

Further on, the kinetic energy functional for non-interacting electrons $T_s[\rho]$ and the Coulomb repulsion including self-interaction $J[\rho]$ is added and subtracted from the energy functional, which is then rewritten as

$$E[\rho] = T_s[\rho] + J[\rho] + E_{xc}[\rho] + \int v(\vec{r})\rho(\vec{r})\, d^3r. \tag{2.7}$$

where the exchange–correlation functional is defined as

$$E_{xc}[\rho] = T[\rho] - T_s[\rho] + V_{ee}[\rho] - J[\rho] \tag{2.8}$$

and

$$J[\rho] = \frac{1}{2}\int \rho(\vec{r})\frac{1}{|\vec{r}-\vec{r}_2|}\rho(\vec{r}_2)\, d^3r\, d^3r_2. \tag{2.9}$$

Then the kinetic energy for non-interacting electrons can be calculated using so called Kohn–Sham (KS) orbitals ϕ_k:

$$T_s[\rho] = \frac{-\hbar^2}{2m_e}\sum_k \langle\phi_k|\nabla^2|\phi_k\rangle. \tag{2.10}$$

The Kohn–Sham orbitals are just a set of auxiliary orthonormal functions yielding the density

$$\rho = \sum_k |\phi_k|^2 \tag{2.11}$$

and do not have a physical meaning in the interacting system [34]. The Coulomb repulsion including self-interaction $J[\rho]$ and the exchange–correlation $E_{xc}[\rho]$ can be directly evaluated from the density and, in principle, does not require the Kohn–Sham orbitals. All functionals are now simple except the exchange–correlation functional $E_{xc}[\rho]$, which includes all the complicated terms and is unknown.

A few approximations for the exchange–correlation are reviewed in the next subsection, but before that let us assume that the exchange–correlation functional is known. Then the Kohn–Sham orbitals can be solved from the following differential equations

$$\left[\frac{-\hbar^2}{2m_e}\nabla^2 + v_{eff}(\vec{r})\right]\phi_k(\vec{r}) = \varepsilon_k \phi_k(\vec{r}), \tag{2.12}$$

where the effective potential is

$$v_{eff}(\vec{r}) = v(\vec{r}) + \int \frac{\rho(\vec{r}_2)}{|\vec{r} - \vec{r}_2|}\, d^3r_2 + v_{xc}(\vec{r}) \tag{2.13}$$

and the Kohn–Sham orbitals are required to be orthonormal

$$\langle \phi_i | \phi_j \rangle = \delta_{ij}. \tag{2.14}$$

The exchange–correlation potential $v_{xc}(\vec{r})$ is obtained from the exchange–correlation functional by taking the functional derivative with respect to the density

$$v_{xc}(\vec{r}) = \frac{\delta E_{xc}[\rho]}{\delta \rho(\vec{r})}. \tag{2.15}$$

The obtained orbital equations are one-particle Schrödinger equations with effective potentials, which are relatively easy to solve, at least when compared to a many-body Schrödinger equation.

2.2.1 Exchange–correlation

The exchange–correlation functional accounts for all quantum mechanical many-body effects of the system: the exchange and the correlation in the kinetic and potential energy. It should also remove the self-interaction in the Coulomb repulsion. The exact form of the functional is unknown and it must be approximated. For the electronic system, the simplest modern approximation for the exchange–correlation functional is the local density approximation (LDA) [34]. At each point the functional is approximated by the functional of a homogeneous electron gas with the density equal to the local density of the system at this point. The exchange–correlation functional of the local density approximation is

$$E_{xc}^{LDA}[\rho] = \int \rho(\vec{r})\, \varepsilon_{xc}^{LDA}(\rho(\vec{r}))\; d^3r \tag{2.16}$$

where $\varepsilon_{xc}^{LDA}(\rho) = \varepsilon_{xc}^{HEG}(\rho)$ is the energy per particle of the homogeneous electron gas (HEG). If the system is spin polarized, the polarization should be taken into account using the local spin density approximation (LSDA). The LSDA exchange–correlation functional is

$$E_{xc}^{LSDA}[\rho_\alpha, \rho_\beta] = \int \rho(\vec{r})\varepsilon_{xc}^{LSDA}(\rho(\vec{r}), \zeta(\vec{r}))\; d^3r, \tag{2.17}$$

where $\zeta = (\rho_\alpha - \rho_\beta)/\rho$ is the spin polarization parameter.

To evaluate the functionals, the exchange and correlation parts can be separated. The exchange functional of a homogeneous electron gas is exactly known, whereas the correlation is not, but a very accurate approximation was developed by Vosko, Wilk, and Nusair [35] based on the quantum Monte Carlo calculations of Ceperley and Adler [36]. For details of the functional see Appendix A.1. Because of the locality of the functionals, they are accurate only for systems where the density changes smoothly, *i.e.*, the local density is close to the density of the surroundings. The local spin density approximation is still frequently used in solid state physics, whereas it is usually insufficient for quantum chemistry.

The local density and spin density approximations can, of course, be improved. The generalized gradient approximations (GGA) include gradients of the spin densities and are thus no longer strictly local, but include some finite range contribution [34]. The meta and hyper–GGAs go even further including Laplacians of the spin densities, Kohn–Sham orbital kinetic energy densities, and even the exact exchange (hyper–GGA) terms [34]. These perform generally better than the strictly local approximations and are sufficient for many quantum chemical applications, but are also increasingly complex.

The density functionals, at least LSDA and GGAs, work generally better for a large number of particles. If a system has only a few electrons, the cancellation of the self-interaction in the Coulomb repulsion by the exchange–correlation functional is poor and it becomes the major source of error. In this case, a simple cure is to remove the self-interaction as proposed by Perdew and Zunger [37]. In this procedure, the self-interaction of each occupied orbital is subtracted from the (LSDA) functional of the whole system

$$E_{xc}^{SIC}[\rho_\alpha,\rho_\beta] = E_{xc}^{LSDA}[\rho_\alpha,\rho_\beta] - \sum_k \left(J[|\phi_k|^2]) + E_{xc}^{LSDA}[|\phi_k|^2, 0] \right) . \quad (2.18)$$

The standard interpretation of the spin density functional theory provides the ground state density $\rho(\vec{r})$, the total energy $E[\rho]$, and the spin magnetization density $m(\vec{r}) = n_\uparrow(\vec{r}) - n_\downarrow(\vec{r})$. For the LSDA and GGA functionals, this interpretation implies unphysical spin densities for some systems. For example, in stretched homonuclear molecules, which dissociate to open shell atoms, more spin-up density is localized on one of the atoms and more spin-down on the other, instead of the correct unpolarized situation. Perdew *et al.* presented an alternative interpretation for the spin density functional theory [38], in which, instead of the spin magnetization density, the on-top electron pair-density is obtained. The on-top electron pair-density is an even function of the two variables $n_\uparrow(\vec{r})$ and $n_\downarrow(\vec{r})$, which are no longer regarded as the spin densities, but are auxiliary variables just as the Kohn–Sham orbitals are. This interpretation does not encounter the spin symmetry dilemma; however, the energy functional is the same as with the standard interpretation. Thus the alternative interpretation is a justification for the use of the unrestricted Kohn–Sham formalism in all systems.

Finally, a remark about the exchange–correlation functionals for time-dependent electronic systems follows. If the time-dependent external potential changes so slowly that the electronic system will remain relaxed at all times, *i.e.*, the system changes adiabatically, one can use the functionals for time-independent systems without modifications [32]. If LDA is used in time-dependent density functional theory, it is called the adiabatic local density approximation (ALDA) and it has been used successfully in many applications. For non-adiabatic processes more advanced functionals must be found.

2.3 Superfluid ^{4}He

The first attempts to model superfluid helium using density functional approach was developed by Gross [39,40] and Pitaevskii [41]. As the superfluid ^{4}He is a bosonic system and all the particles are in the same quantum state, the non-interacting kinetic energy can be obtained directly from the density. In the Gross–Pitaevskii (GP) functional, everything else is included in one non-linear interaction term, which is directly proportional to the square of the local density:

$$E^{GP}[\rho] = \int |\nabla\sqrt{\rho(\vec{r})}|^2\, d^3r + \int g|\rho(\vec{r})|^2\, d^3r. \tag{2.19}$$

If the total energy is shifted by $-N\mu = -Ng\rho_0$, where μ is the energy per particle in the ground state, then

$$E^{GP}[\rho] = \int |\nabla\sqrt{\rho(\vec{r})}|^2\, d^3r + \int g\rho(\vec{r})(\rho(\vec{r}) - \rho_0)\, d^3r. \tag{2.20}$$

From the above equation, it can been seen that the energy increases if the density is non-uniform or it differs from the ground state density ρ_0. The functional has been successfully used to model, for example, vortices in superfluid [42], but it has its restrictions. As the functional is local, it can be applied only to systems where the density varies slowly. In addition, as it does not yield a surface tension and produces incorrect surface structures, it is unsuitable for atomic scale systems.

Many functionals [43–46] have been developed to improve the Gross–Pitaevskii functional, of which one of the most advanced is the Orsay–Trento (OT) functional [46]. It is a phenomenological functional, *i.e.*, each term is based on a physical phenomenon, which determines the form of a term, but the parameters in the term are determined by fitting to experimental data. The Orsay–Trento energy functional for time-independent systems is

$$\begin{aligned} E^{OT}[\rho] = &\int |\nabla\sqrt{\rho(\vec{r})}|^2\, d^3r \\ &+ \frac{1}{2}\int\int \rho(\vec{r}_1)V_l(|\vec{r}_1 - \vec{r}_2|)\rho(\vec{r}_2)\, d^3r_1\, d^3r_2 \\ &+ \frac{c_2}{2}\int \rho(\vec{r})(\bar{\rho}(\vec{r}))^2\, d^3r + \frac{c_3}{3}\int \rho(\vec{r})(\bar{\rho}(\vec{r}))^3\, d^3r \\ &- \frac{\hbar^2}{4m}\alpha_s \int\int F(|\vec{r}_1 - \vec{r}_2|)\times \\ &\qquad \left(1 - \frac{\tilde{\rho}(\vec{r}_1)}{\rho_{0s}}\right)\nabla\rho(\vec{r}_1)\cdot\nabla\rho(\vec{r}_2)\left(1 - \frac{\tilde{\rho}(\vec{r}_2)}{\rho_{0s}}\right)\, d^3r_1\, d^3r_2. \end{aligned} \tag{2.21}$$

The first term in (2.21) is the same non-interacting kinetic energy as in the Gross–Pitaevskii functional. The second term is a finite-range pair-interaction, in which the Lennard-Jones pair-potential is screened at close distances to remove the self-interaction

$$V_l(r) = \begin{cases} 0, & \text{if } r < h \\ 4\varepsilon\left[\left(\frac{\sigma}{r}\right)^{12} - \left(\frac{\sigma}{r}\right)^{6}\right], & \text{if } r \geq h \end{cases} \tag{2.22}$$

with the screening distance $h = 2.1903$ Å, hard-core radius $\sigma = 2.556$ Å and well-depth $\varepsilon = 10.22$ K (Figure 2.1).

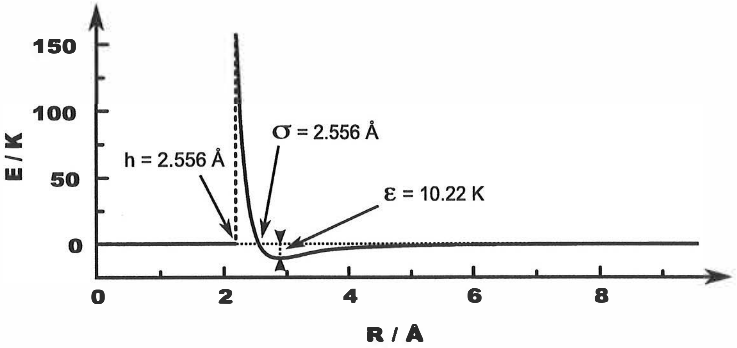

Figure 2.1: Lennard–Jones pair-potential, which is screened at close distances to remove self-interaction.

The short range many-body correlations are accounted for by the third and fourth terms of Eq. (2.21), which are a kind of three- and four-body contact-interactions, respectively,

$$\frac{c_2}{2}\int \rho(\vec{r})(\overline{\rho}(\vec{r}))^2\, d^3r = \frac{c_2}{2}\int\int\int \delta(|\vec{r}_1 - \vec{r}_2|)\delta(|\vec{r}_1 - \vec{r}_3|)\delta(|\vec{r}_2 - \vec{r}_3|)\times \rho(\vec{r}_1)\overline{\rho}(\vec{r}_2)\overline{\rho}(\vec{r}_3)\, d^3r_1\, d^3r_2\, d^3r_3, \tag{2.23}$$

and

$$\begin{aligned} &\frac{c_3}{3}\int \rho(\vec{r})(\overline{\rho}(\vec{r}))^3\, d^3r \\ &\quad = \frac{c_3}{3}\int\int\int\int \delta(|\vec{r}_1 - \vec{r}_2|)\delta(|\vec{r}_1 - \vec{r}_3|)\delta(|\vec{r}_1 - \vec{r}_4|)\times \\ &\qquad \delta(|\vec{r}_2 - \vec{r}_3|)\delta(|\vec{r}_2 - \vec{r}_4|)\delta(|\vec{r}_3 - \vec{r}_4|)\times \\ &\qquad \rho(\vec{r}_1)\overline{\rho}(\vec{r}_2)\overline{\rho}(\vec{r}_3)\overline{\rho}(\vec{r}_4)\, d^3r_1\, d^3r_2\, d^3r_3\, d^3r_4, \end{aligned} \tag{2.24}$$

where the spherical average of the density

$$\overline{\rho}(\vec{r}) = \int \Pi_h(|\vec{r} - \vec{r}_2|)\rho(\vec{r}_2)\, d^3r_2 \tag{2.25}$$

takes the average of the density inside the screening distance h. The parameters h, $c_2 = 2.411857 \times 10^4$ KÅ^6 and $c_3 = 1.858496 \times 10^6$ KÅ^9 are determined from the experimental values of the density, the energy per particle and the compressibility of a uniform system at zero pressure.

The last term in Eq. (2.21) provides a non-local correction to the kinetic energy and its parameters are fixed to reproduce the static linear response function. The static response function $\chi(q)$, which describes the system's response to a small external periodic perturbation, is obtained by taking the second functional derivative of the energy functional with respect to the density in the momentum space (momentum $p = \hbar q$):

$$\begin{aligned}
-\frac{1}{\chi(q)} =& \frac{\hbar^2 q^2}{4m} + \frac{\rho}{V} \int\int \frac{\delta^2 E}{\delta\rho(\vec{r}_1)\delta\rho(\vec{r}_2)} e^{-i\vec{q}\cdot(\vec{r}_1-\vec{r}_2)}\, d^3r_1\, d^3r_2 \\
=& \frac{\hbar^2 q^2}{4m} \\
&+ \rho\hat{V}_l(q) + c_2[2\hat{\Pi}_h(q) + \hat{\Pi}_h^2(q)]\rho^2 + 2c_3[\hat{\Pi}_h(q) + \hat{\Pi}_h^2(q)]\rho^3 \\
&- \frac{\hbar^2}{2m}\alpha_s\rho\left(1 - \frac{1}{\rho_{0s}}\rho\right)^2 q^2 e^{-\frac{1}{4}q^2 l^2},
\end{aligned} \tag{2.26}$$

where $\hat{V}_l(q)$ and $\hat{\Pi}_h(q)$ are Fourier transforms of $V_l(r)$ and $\Pi_h(r)$, respectively. The last line of Eq. (2.26) corresponds to the non-local correction to the kinetic energy, in which terms involving the wavenumber q fix the shape of the static response function (Figure 2.2) and the terms involving density ρ give the correct pressure dependence. The values for parameters are α_s 54.31 Å^3, $\rho_{0s} = 0.04$ Å and $l = 1$ Å. The function $F(r)$ is a Gaussian

$$F(r) = (l\sqrt{\pi})^{-3} e^{-r^2/l^2} \tag{2.27}$$

and $\tilde{\rho}(\vec{r})$ is the density smoothed by the Gaussian $F(r)$

$$\tilde{\rho}(\vec{r}_1) = \int F(|\vec{r}_1 - \vec{r}_2|)\rho(\vec{r}_2)\, d^3r_2. \tag{2.28}$$

This term, the non-local correction to the kinetic energy, contributes mostly to the properties of the functional when the density varies on the interatomic length scale.

The proper treatment of the time-dependent systems requires that the functional can reproduce the dispersion relation in the momentum range accessible by the system. The Orsay–Trento functional reproduces the dispersion relation correctly in the initial phonon branch and it also reproduces the

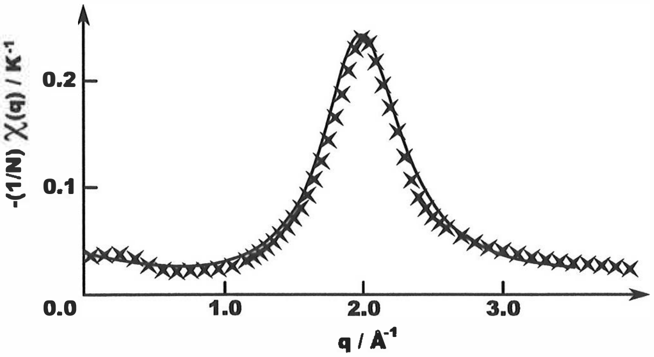

Figure 2.2: Static response function for superfluid ^{4}He. Reproduced from [46]. Crosses, experimental data; solid line, the Orsay–Trento functional.

maxon and the roton minimum qualitatively, but these are shifted by more than 5 K up in energy. This shift appears due to the lack of a backflow in the functional. The backflow reduces the energy of the maxon–roton region by introducing new currents, which, for example, allow the rotons to satisfy the mass conservation law without variations in the density (Figure 2.3).

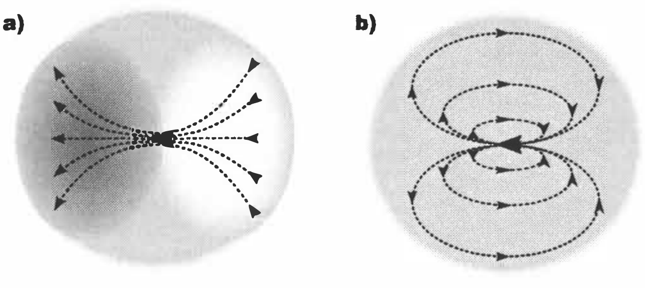

Figure 2.3: Sketch of a roton wave packet a) without backflow and b) with backflow. Dashed line, current; Greyscale background, density.

The backflow is included into the Orsay–Trento functional by two velocity dependent terms

$$\int \frac{1}{2} m\rho(\vec{r})|\vec{v}(\vec{r})|^2 \, d^3r - \frac{m}{4} \int \int V_J(|\vec{r} - \vec{r}_2|)\rho(\vec{r})\rho(\vec{r}_2) \, |\vec{v}(\vec{r}) - \vec{v}(\vec{r}_2)|^2 \, d^3r \, d^3r_2, \tag{2.29}$$

which are the diagonal terms of the most general quadratic form for the backflow [46]. The first term is just the hydrodynamic kinetic energy, whereas the second term is the nonlocal current–current interaction. The current-

current interaction potential $V_J(r)$ has been parametrized as

$$V_J(r) = (\gamma_{11} + \gamma_{12} r^2) e^{-\alpha_1 r^2} + (\gamma_{21} + \gamma_{22} r^2) e^{-\alpha_2 r^2}, \tag{2.30}$$

where $\gamma_{11} = -19.7544$, $\gamma_{21} = -0.2395$, $\gamma_{12} = 12.5616$ Å^{-2}, $\gamma_{22} = 0.0312$ Å^{-2}, $\alpha_1 = 1.023$ Å^{-1}, and $\alpha_2 = 0.14912$ Å^{-1} have been fixed to reproduce the dispersion relation:

$$[\hbar\omega(q)]^2 = \frac{\hbar^2 q^2}{m|\chi(q)|} \left\{ 1 - \rho \left[\hat{V}_J(0) - \hat{V}_J(q) \right] \right\}, \tag{2.31}$$

where $\hat{V}_J(q)$ is the Fourier transform of $V_J(r)$. The backflow term vanishes for the ground state and it does not contribute to the static response. Thus no modifications are required for the other terms and the backflow must be included only for time-dependent systems.

Chapter 3

Quantum Monte Carlo methods

The quantum Monte Carlo methods are based on the statistical sampling of the 3N–dimensional space. Instead of trying to solve the Schrödinger equation of a many-body system, the expectation values of the desired operators are evaluated using the random sampling of the 3N–dimensional space in a fashion closely related to the Monte Carlo integration. Actually, the variational Monte Carlo is just one way of performing the Monte Carlo integration for the expectation values of a trial wavefunction.

3.1 Variational Monte Carlo

The variational Monte Carlo (VMC) method itself does not optimize the trial wavefunction; it just provides the expectation value of an operator, usually the energy, corresponding to the given trial wavefunction. The optimization of the trial wavefunction has to be done by other means. The VMC method just produces a set of random samples from the trial wavefunction for the Monte Carlo integration of the expectation value. In its simplest form, it takes an average of the local values $f(\vec{R}_i)$ at random points $\vec{R}_i$, which are uniformly distributed over space:

$$F = \int f(\vec{r})\, d^3r = \frac{1}{M}\sum_i^M f(\vec{R}_i) + \mathcal{O}(\sqrt{M}) \tag{3.1}$$

This chapter is essentially based on reference [47].

which is for the energy

$$
\begin{aligned}
E_{VMC} =& \frac{\langle\psi_T|\hat{H}|\psi_T\rangle}{\langle\psi_T|\psi_T\rangle} \\
=& \frac{1}{M}\sum_i^M \langle\psi_T(\vec{R}_i)|\hat{H}|\psi_T(\vec{R}_i)\rangle + \mathcal{O}(\sqrt{M}) \\
=& \frac{1}{M}\sum_i^M E_L(\vec{R}_i)|\psi_T(\vec{R}_i)|^2 + \mathcal{O}(\sqrt{M}),
\end{aligned}
\tag{3.2}
$$

where the local energy is

$$
E_L(\vec{R}_i) = \frac{\hat{H}\psi_T(\vec{R}_i)}{\psi_T(\vec{R}_i)}, \tag{3.3}
$$

$\psi_T(\vec{R})$ is the trial wavefunction, and $\vec{R}_i = (\vec{r}_1^{\,(i)}, \vec{r}_2^{\,(i)}, ..., \vec{r}_n^{\,(i)})$ is a random vector with an uniform distribution in space. The error is reduced quite slowly $\mathcal{O}(\sqrt{M})$ as the number of samples is increased, however, the error does not depend on the degrees of freedom in the system, which makes the method useful for a large number of particles.

However, the uniform sampling is quite inefficient, as the whole infinite space is sampled uniformly, but the major contribution to the expectation value arises only from the areas where the trial wavefunction has a significant amplitude. An obvious solution is to use a weighted random distribution instead of a uniform one to increase the average weight $|\psi_T(\vec{R})|^2$ and thus increase the efficiency. If one could produce a random distribution weighted by $|\psi_T(\vec{R})|^2$, each sample would have an optimal, *i.e.*, equal, contribution to the energy expectation value

$$
E_{VMC} = \frac{1}{M}\sum_i^M E_L(\vec{Q}_i) + \mathcal{O}(\sqrt{M}), \tag{3.4}
$$

where $\vec{Q}_i$ is a random vector with distribution $|\psi_T(\vec{R})|^2$. This is exactly what can be done using the Metropolis–sampling.

3.1.1 Metropolis–sampling

One way to produce a random sample from a distribution $f(\vec{R})$ is to use the concept of random walking. A walker, which is a configuration of all particles (not a particle itself) in a system, is moved from one configuration

$\vec{Q}_i$ to another configuration $\vec{Q}_{i+1}$ with some probability $G(\vec{Q}_{i+1}, \vec{Q}_i)$. To produce the distribution $f(\vec{R})$ the probability $G(\vec{Q}_{i+1}, \vec{Q}_i)$ must be chosen in such a way that, when the distribution $f(\vec{R})$ is reached, an equal number of walkers move from $\vec{Q}_i$ to $\vec{Q}_{i+1}$ as moves from $\vec{Q}_{i+1}$ to $\vec{Q}_i$

$$G(\vec{Q}_{i+1}, \vec{Q}_i) f(\vec{Q}_i) = G(\vec{Q}_i, \vec{Q}_{i+1}) f(\vec{Q}_{i+1}). \tag{3.5}$$

In the Metropolis–sampling the probability is chosen to be unity if the new configuration is more probable than the old, and else it is the ratio $f(\vec{Q}_{i+1})/f(\vec{Q}_i)$, *i.e.*, the probability is

$$G(\vec{Q}_{i+1}, \vec{Q}_i) = \min\left(1, \frac{f(\vec{Q}_{i+1})}{f(\vec{Q}_i)}\right). \tag{3.6}$$

This defines the probability for moving from $\vec{Q}_i$ to $\vec{Q}_{i+1}$, however; it does not define how the move is performed, *i.e.*, how $\vec{Q}_{i+1}$ is chosen, which will be discussed in the next section.

There are two requirements for the random walk to produce an equilibrium distribution. From all configurations $\vec{Q}$ there must be a possible route to all other configurations $\vec{R}$, *i.e.*, $G(\vec{R}, \vec{Q}) > 0$ for all $\vec{Q}$ and $\vec{R}$, which includes the possibility to stay at the current configuration $\vec{Q}$, *i.e.*, $G(\vec{Q}, \vec{Q}) > 0$ for all $\vec{Q}$. Otherwise, the walkers may not sample one or more separated regions of the configuration space as there is no continuous path from one region to another. Moreover, the walkers may remain in a correlated cyclic motion infinitely, if there is "friction", *i.e.*, a possibility to stay at the current configuration (see figure 3.1).

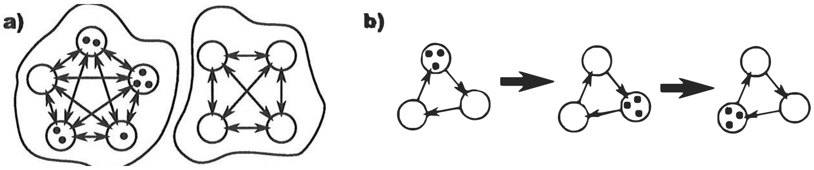

Figure 3.1: Illustrations of systems possessing improper random walks: a) unconnected regions and b) a cyclic system without "friction".

3.1.2 Importance sampling

The simplest way to generate moves for a walker tied a given probability $G(\vec{Q}_{i+1}, \vec{Q}_i)$ is, to first introduce a move with a uniform distribution inside some finite range δ, and then accept it with a probability $G(\vec{Q}_{i+1}, \vec{Q}_i)$. If the move is accepted, the new position for the walker is $\vec{Q}_{i+1}$. If it is not, the walker remains in its old position, *i.e.*, the new position $\vec{Q}_{i+1}$ is equal to the old position $\vec{Q}_i$. This is still not very efficient because many of the moves will be towards undesired directions and will not be accepted. To improve the acceptance ratio, one must guide the walkers towards directions where the amplitude of the wavefunction increases. This is called importance sampling.

In the importance sampling, steps to different configurations are associated with unequal transition probabilities. The total probability for a move is the product of the transition probability $T(\vec{Q}_{i+1}, \vec{Q}_i)$ and the acceptance probability $A(\vec{Q}_{i+1}, \vec{Q}_i)$

$$G(\vec{Q}_{i+1}, \vec{Q}_i) = T(\vec{Q}_{i+1}, \vec{Q}_i)A(\vec{Q}_{i+1}, \vec{Q}_i). \tag{3.7}$$

The transition probability can be derived from the time-dependent Schrödinger equation of an auxiliary system, in which the ground state is equal to the trial wavefunction ψ_T (see Appendix A.2). The result of this derivation is a diffusion equation for a time-dependent distribution $f(\vec{R}, \tau)$

$$\frac{\partial f(\vec{R}, \tau)}{\partial \tau} = D\nabla^2 f(\vec{R}, \tau) - D\nabla \cdot \left[f(\vec{R}, \tau)\vec{F}_Q(\vec{R})\right], \tag{3.8}$$

where $\vec{F}_Q((\vec{R}) = 2\frac{\nabla\psi_T(\vec{R})}{\psi_T(\vec{R})}$ is the quantum force guiding walkers towards regions where the trial wavefunction has a large amplitude. As the imaginary time τ approaches infinity, the distribution approaches the density of the trial wavefunction $f(\vec{R}, \tau \to \infty) \to |\psi_T(\vec{R})|^2$. If the time step $\delta\tau$ is small, the quantum force is essentially unchanged between the initial and final configurations; then, to satisfy the diffusion equation (3.8), the new configurations are obtained by

$$\vec{R}(\tau + \delta\tau) = \vec{R}(\tau) + D\vec{F}_Q(\vec{R}(\tau))\delta\tau + \vec{\chi}(D, \delta\tau), \tag{3.9}$$

where $\vec{\chi}(D, \delta\tau)$ is a random Gaussian vector with a zero mean and a variance of $2D\delta\tau$. The corresponding transition probability is

$$\begin{aligned} &T(\vec{Q}_{i+1}, \vec{Q}_i; \delta\tau) = \\ &\qquad (4\pi D\delta\tau)^{-3N/2} \exp\left[-\left(\vec{Q}_{i+1} - \vec{Q}_i - D\delta\tau\vec{F}_Q(\psi_T(\vec{Q}))\right)^2 / 4D\delta\tau\right], \end{aligned} \tag{3.10}$$

where $\vec{Q}_i = \vec{R}(\tau)$ and $\vec{Q}_{i+1} = \vec{R}(\tau + \delta\tau)$.

However, when the time step $\delta\tau$ is finite, the quantum force is not exactly unchanged and thus the diffusion equation (3.8) is not exactly reproduced by the random walk of Eq. (3.9). This can be corrected by the Metropolis–sampling for the acceptance probability

$$A(\vec{Q}_{i+1}, \vec{Q}_i; \delta\tau) = \min\left(1, \frac{T(\vec{Q}_i, \vec{Q}_{i+1}; \delta\tau)|\psi_T(Q_{i+1})|^2}{T(\vec{Q}_{i+1}, \vec{Q}_i; \delta\tau)|\psi_T(Q_i)|^2}\right), \tag{3.11}$$

which rejects some of the proposed moves to restore the correct total probability $G(\vec{Q}_{i+1}, \vec{Q}_i)$.

To summarize, in the importance sampled variational Monte Carlo, a sampling step begins by an introduction of a possible change in the configuration by a guided random vector. The Metropolis–sampling gives the acceptance probability, and the move is either accepted and the walker is moved to this new configuration, or the move is rejected and the walker stays in the old configuration. Finally, the local value of an observable is evaluated in the current position. The sampling procedure is repeated, usually for a set of walkers, until an equilibrium distribution is reached and enough samples are recorded for an accurate estimate for the expectation value. The cost to pay for the importance sampling is that one has to evaluate the quantum force in each visited configuration; however, the overall efficiency usually increases.

3.2 Diffusion Monte Carlo

The variational Monte Carlo can be used only to evaluate the expectation values of the trial wavefunction and the optimization of the wavefunction must be done by other means. The diffusion Monte Carlo can be considered as an improvement to the variational Monte Carlo as it uses the available knowledge about the system, *i.e.*, the Hamiltonian, to improve the expectation value. The partial differential equation, similar to the diffusion equation of the variational Monte Carlo, can be derived by using two different systems: the system under examination and an auxiliary system with the trial wavefunction as its ground state wavefunction (see Appendix A.2). The resulting equation is

$$\begin{aligned}\frac{\partial f(\vec{R}, \tau)}{\partial \tau} = D\nabla^2 f(\vec{R}, \tau) - D\nabla \cdot \left[f(\vec{R}, \tau)\vec{F}_Q(\vec{R})\right] \\ + (E_T - E_L(\vec{R}))f(\vec{R}, \tau),\end{aligned} \tag{3.12}$$

where the distribution $f(\vec{R},\tau) = \phi(\vec{R},\tau)\psi_T(\vec{R})$ and E_T is the ground state energy of the auxiliary system. The first two terms on the right-hand side of Eq. (3.12) are equal to the right-hand side of the VMC diffusion equation, Eq. (3.8). The third term on the right-hand side corresponds to branching, and wherever it is above zero, the distribution will grow in time, and wherever it is below zero, the distribution is decaying. These two processes, diffusion and branching, are competing and, as a result, as the imaginary time τ approaches infinity, the distribution approaches the product of the ground state wavefunction and the trial wavefunction, $f(\vec{R},\tau \to \infty) \to \phi_0(\vec{R})\psi_T(\vec{R})$. Since the distribution now includes the ground state wavefunction, the expectation value of the energy *is* the ground state energy

$$E_{DMC} = \frac{\langle\phi_0|\hat{H}|\psi_T\rangle}{\langle\phi_0|\psi_T\rangle} = E_0. \tag{3.13}$$

To include the branching into the random walk, the differential equation (3.12) is solved in two stages. In the first stage, only the first two terms of the right-hand side are accounted for by a random move equal to the VMC move. In the second stage, a differential equation, which includes only the branching term, is solved:

$$\begin{aligned}\frac{\partial f(\vec{R},\tau)}{\partial\tau} &= (E_T - E_L(\psi_T(\vec{R}))f(\vec{R},\tau) \\ &\Longrightarrow f(\vec{R},\tau+\delta\tau) = f(\vec{R},\tau)\exp[-(E_L(\psi_T(\vec{R})) - E_T)\delta\tau]. \end{aligned} \tag{3.14}$$

The exponential term can be regarded as the probability of a walker to stay alive. If the probability is larger than unity, then the fraction above unity is the walker's probability to create a copy of itself, *i.e.*, to branch. In practice, it is more appropriate to use the average of the local energy before and after the move

$$f(\vec{Q}_{i+1},\tau+\delta\tau) = f(\vec{Q},\tau)\exp\left\{-\left[\frac{E_L(\psi_T(\vec{Q}_i)) + E_L(\psi_T(\vec{Q}_{i+1}))}{2} - E_T\right]\delta\tau\right\}, \tag{3.15}$$

because it reduces the order of error in expectation values when the time step $\delta\tau$ is finite. The source of the error is the inexact solution of the partial differential equation (3.12), as it is solved in two stages.

To summarize, the diffusion Monte Carlo provides, directly without optimization, the ground state energy as well as improved approximations for other expectation values, but it has a time step bias. The sampling step of the diffusion Monte Carlo is otherwise equal to that of variational Monte Carlo, but the branching can kill the walker or breed new walkers. Typically, the variational Monte Carlo is used in the optimization of the trial wavefunction, and the final results are then obtained from a diffusion Monte Carlo calculation with the optimized trial wavefunction.

Chapter 4

Numerical implementation

This chapter[*] describes the numerical implementation of computer programs developed in this work. The first program was designed to model both time-independent and time-dependent systems using the density functional theory. Currently, the local spin density functional [34] for electronic systems and the Orsay–Trento functional [46] for superfluid ^{4}He are implemented in the program, which is easily extendable for other functionals. In the first section 4.1, a method for time-dependent systems is described, which is then modified in the second section 4.2 for time-independent systems. The last section 4.3 introduces the main design considerations of a variational and diffusion Monte Carlo program.

4.1 Time-dependent density functional theory – semi-implicit time propagation

The numerical solution of a time-dependent problem by the density functional theory requires a solution for a set of coupled, non-linear partial dif-

---

[*] This chapter is mainly based on papers II and IV.

ferential equations, *i.e.*, time-dependent Kohn-Sham equations

$$\begin{aligned}
i\hbar\frac{\partial\psi_1(\vec{r},t)}{\partial t} &= \hat{H}[\psi_1,\psi_2,...\psi_n]\psi_1(\vec{r},t)\\
i\hbar\frac{\partial\psi_2(\vec{r},t)}{\partial t} &= \hat{H}[\psi_1,\psi_2,...\psi_n]\psi_2(\vec{r},t)\\
&\dots\\
i\hbar\frac{\partial\psi_n(\vec{r},t)}{\partial t} &= \hat{H}[\psi_1,\psi_2,...\psi_n]\psi_n(\vec{r},t).
\end{aligned} \tag{4.1}$$

To discretize these equations for the computer implementation, a basis set needs to be defined. A basis composed of Gaussian functions, which is extensively used in quantum chemistry, is not the best choice for all problems. The Gaussian basis works well when orbitals can be reproduced relatively accurately with a limited number of basis functions. In principle, the Gaussian basis could be used to represent any orbital, but in practice, finite precision (computer) arithmetics causes numerical instabilities when an extensive set of nearly linearly dependent Gaussians is used. This was observed in the present studies, for example, when two electrons occupied the same cavity in superfluid helium. The instabilities caused by the linear dependency do not occur with orthogonal bases (or bases with weak support) like a plane wave basis or an equidistant, real-space, Cartesian grid. It is noteworthy that these are actually the same basis in different spaces: momentum and spatial spaces, respectively. These bases can reproduce virtually any wavefunction if sufficiently many basis functions are used. In addition to flexibility, the grid bases have an advantage that these lead to sparse matrices and a simple, efficient parallel execution is easy to achieve. The drawback is that a huge number of basis functions is usually needed.

4.1.1 Semi-implicit propagators

The next important choice after the basis is how to propagate the wavefunctions as the effective Hamiltonian is coupled and non-linear. The simplest choice would assume the Hamiltonian to be essentially unchanged during an iteration step and use the explicit Euler propagation:

$$\psi(t+\Delta t) = \left(1 - \frac{i}{\hbar}H[\psi_1(t),\psi_2(t),...,\psi_n(t)]\Delta t + \mathcal{O}(\Delta t^2)\right)\psi(\vec{r},t). \tag{4.2}$$

However, this propagator is unconditionally unstable and therefore of only limited use. The implicit Euler is unconditionally stable in a linear case, but not necessarily in a non-linear case as one can not form the Hamiltonian at the end of the iteration step, at time $t + \Delta t$. Again, the first approximation would be to assume that the Hamiltonian is essentially unchanged and use the Hamiltonian at the beginning of the iteration step, at time t:

$$\left(1 + \frac{i}{\hbar} H[\psi_1(t), \psi_2(t), ..., \psi_n(t)]\Delta t + \mathcal{O}(\Delta t^2)\right) \tilde{\psi}(t + \Delta t) = \psi(t). \tag{4.3}$$

Now, the approximation of the Hamiltonian can be improved by utilizing the new wavefunctions $\tilde{\psi}(t + \Delta t)$ obtained in the current iteration. The old wavefunctions are propagated again employing the improved approximation of the Hamiltonian:

$$\begin{aligned} \left(1 + \frac{i}{\hbar} H[\psi_1(t), ..., \psi_n(t)]\Delta t + \mathcal{O}(\Delta t^2)\right) \tilde{\psi}(t + \Delta t) &= \psi(t) \\ \left(1 + \frac{i}{\hbar} H[\tilde{\psi}_1(t + \Delta t), ..., \tilde{\psi}_n(t + \Delta t)]\Delta t + \mathcal{O}(\Delta t^2)\right) \psi(t + \Delta t) &= \psi(t). \end{aligned} \tag{4.4}$$

This semi-implicit scheme is in fact a kind of a predictor–corrector scheme or a self-consistent field iteration with only one iteration step. The predictor step uses a Hamiltonian evaluated from first-order accurate wavefunctions, $\psi(t) = \psi(t + \Delta t) + \mathcal{O}(\Delta t)$, whereas the corrector step uses a Hamiltonian evaluated from second-order accurate wavefunctions, $\tilde{\psi}(t+\Delta t) = \psi(t+\Delta t) + \mathcal{O}(\Delta t^2)$. Any further corrector steps would not improve the order of accuracy of the wavefunction used in the evaluation of the Hamiltonian. Thus, it is more efficient to reduce the time step rather than increase the number of corrector steps.

The accuracy of the time propagation can be further improved by using a semi-implicit Crank–Nicolson propagator

$$\begin{aligned} \left(1 + \frac{i}{\hbar} H[\psi_1(t), ..., \psi_n(t)]\Delta t + \mathcal{O}(\Delta t^2)\right) \tilde{\psi}(t + \Delta t) & \\ = \left(1 - \frac{i}{\hbar} H[\psi_1(t), ..., \psi_n(t)]\Delta t\right) \psi(t) & \\ \left(1 + \frac{i}{\hbar} H[t + \Delta t/2]\Delta t + \mathcal{O}(\Delta t^3)\right) \psi(t + \Delta t) & \\ = \left(1 - \frac{i}{\hbar} H[t + \Delta t/2]\Delta t\right) \psi(t), & \end{aligned} \tag{4.5}$$

where the Hamiltonian in the middle of the step is approximated by

$$H[t+\Delta t/2] \approx \frac{1}{2}H[\tilde{\psi}_1(t), ..., \tilde{\psi}_n(t)] + \frac{1}{2}H[\psi_1(t), ..., \psi_n(t)]. \tag{4.6}$$

If the nonlinear Hamiltonian itself is accurate to at least the second-order when evaluated using second-order accurate wavefunctions, then the method is also second-order accurate (see Appendix A.3). Even if it is not, but the error is relatively small, it is nearly second-order accurate and thus superior to the Euler methods, at least in practice.

4.1.2 Operator splitting

The semi-implicit propagators introduced above lead to a set of linearized matrix equations. If the real-space grid basis is used, the Laplacians and possible gradients in the Hamiltonian must be approximated. This can be done using, for example, the second-order finite difference approximation, which is for the Laplacian

$$\begin{aligned}\nabla^2\psi(x,y,z) = {} & \frac{\psi(x-\Delta,y,z) - 2\psi(x,y,z) + \psi(x+\Delta,y,z)}{\Delta^2} \\ & + \frac{\psi(x,y-\Delta,z) - 2\psi(x,y,z) + \psi(x,y+\Delta,z)}{\Delta^2} \\ & + \frac{\psi(x,y,z-\Delta) - 2\psi(x,y,z) + \psi(x,y,z+\Delta)}{\Delta^2} \\ & + \mathcal{O}(\Delta^2) \end{aligned} \tag{4.7}$$

and for the gradient

$$\begin{aligned}\nabla\psi(x,y,z) = {} & \frac{\psi(x+\Delta,y,z) - \psi(x-\Delta,y,z)}{2\Delta}\hat{e}_x \\ & + \frac{\psi(x,y+\Delta,z) - \psi(x,y-\Delta,z)}{2\Delta}\hat{e}_y \\ & + \frac{\psi(x,y,z+\Delta) - \psi(x,y,z-\Delta)}{2\Delta}\hat{e}_z \\ & + \mathcal{O}(\Delta^2). \end{aligned} \tag{4.8}$$

The resulting Hamiltonian matrix is sparse and could be solved, for example, by applying sparse matrix techniques like the conjugate gradient method, but it is more efficient to exploit the operator splitting method. The operator splitting method is used to separate strongly non-diagonal parts (*e.g.* kinetic energy terms) and diagonal or weakly non-diagonal parts (*e.g.* the potential terms). This is done by first formally solving the time-dependent Schrödinger equation:

$$i\hbar\frac{\partial\psi}{\partial t} = \hat{H}\psi \quad \Longrightarrow \quad \psi(t+\Delta t) = \exp[-i\hat{H}\Delta t/\hbar]\psi(t) \tag{4.9}$$

and then separating the kinetic and potential terms of the operator

$$\exp[-i\hat{H}\Delta t/\hbar] = \exp[-i\hat{T}\Delta t/2\hbar]\exp[-i\hat{V}\Delta t/\hbar]\exp[-i\hat{T}\Delta t/2\hbar] + \mathcal{O}(\Delta t^3). \tag{4.10}$$

Furthermore, the operator splitting allows one to evaluate each Cartesian component of the kinetic energy operator separately:

$$\exp[-i\hat{T}\Delta t/\hbar] = \exp[-i\hat{T}_x\Delta t/\hbar]\exp[-i\hat{T}_y\Delta t/\hbar]\exp[-i\hat{T}_z\Delta t/\hbar] \tag{4.11}$$

and

$$\begin{aligned}\exp[-i\hat{H}\Delta t/\hbar] = {} & \exp[-i\hat{T}_x\Delta t/2\hbar]\exp[-i\hat{T}_y\Delta t/2\hbar]\exp[-i\hat{T}_z\Delta t/2\hbar] \\ & \times \exp[-i\hat{V}\Delta t/\hbar] \\ & \times \exp[-i\hat{T}_z\Delta t/2\hbar]\exp[-i\hat{T}_y\Delta t/2\hbar]\exp[-i\hat{T}_x\Delta t/2\hbar] \\ & + \mathcal{O}(\Delta t^3),\end{aligned} \tag{4.12}$$

as the components commute with each other. Now, the solution can be obtained by solving the following set of equations:

$$\begin{aligned}\psi^{(1)}(t+\Delta t) &= \exp[-i\hat{T}_x\Delta t/2\hbar]\psi(t) \\ \psi^{(2)}(t+\Delta t) &= \exp[-i\hat{T}_y\Delta t/2\hbar]\psi^{(1)}(t+\Delta t) \\ \psi^{(3)}(t+\Delta t) &= \exp[-i\hat{T}_z\Delta t/2\hbar]\psi^{(2)}(t+\Delta t) \\ \psi^{(4)}(t+\Delta t) &= \exp[-i\hat{V}\Delta t/\hbar]\psi^{(3)}(t+\Delta t) \\ \psi^{(5)}(t+\Delta t) &= \exp[-i\hat{T}_z\Delta t/2\hbar]\psi^{(4)}(t+\Delta t) \\ \psi^{(6)}(t+\Delta t) &= \exp[-i\hat{T}_y\Delta t/2\hbar]\psi^{(5)}(t+\Delta t) \\ \psi(t+\Delta t) &= \exp[-i\hat{T}_x\Delta t/2\hbar]\psi^{(6)}(t+\Delta t),\end{aligned} \tag{4.13}$$

which are transformed back to corresponding time-dependent Schrödinger equations and solved one after another using the propagators of the previous section, *e.g.*, the (semi-implicit) Crank–Nicolson. Note that it is not necessary to use the semi-implicit propagation for other than the potential propagation, as the kinetic energy equations are linear.

After the operator splitting, all matrices of the operators $\hat{T}_x$, $\hat{T}_y$, $\hat{T}_z$ and $\hat{V}$ are structured. The kinetic energy operators correspond to tridiagonal matrices, or banded matrices, if a higher order finite difference approximation is used, which can be solved extremely efficiently compared to a general sparse matrix. If the potential is real and depends only on the density, the potential propagation changes only the phase of the wavefunction, but not the density. In this case, the potential matrix is effectively diagonal and the semi-implicit treatment is unnecessary. However, if the potential has weak off-diagonal terms, *e.g.*, gradients or Laplacians with small prefactors, or has a small imaginary part, the semi-implicit scheme must be employed to solve the equation accurately. For example, the semi-implicit propagation must be employed for the Orsay–Trento potential. In the case, if the off-diagonal or imaginary parts are not small, the semi-implicit scheme might not be enough. However, these systems are out of the scope of this thesis. The total computational cost for solving the linearized equations with N points per axis on 3D real-space grid reduces from $\mathcal{O}\left((N^3)\sqrt{(N^2)}\right) = \mathcal{O}\left(N^4\right)$ of the iterative solvers [48], to $\mathcal{O}\left(N^3\right)$, when using the operator splitting (and the potential has already been calculated, which is described in 4.1.4).

4.1.3 Exponential propagators

While the potential is effectively diagonal or nearly diagonal in the spatial space, the kinetic energy operator is diagonal in the momentum space, *i.e.*, it is a local multiplication proportional to the square of the wave vector:

$$-\frac{\hbar^2}{2m}\nabla^2\psi(\vec{r}) \longrightarrow \frac{\hbar^2}{2m}|k|^2\tilde{\psi}(\vec{k}), \tag{4.14}$$

where

$$\tilde{\psi}(\vec{k}) = \iiint \psi(x,y,z)e^{-i(k_x x + k_y y + k_z z)}\,dx\,dy\,dz \tag{4.15}$$

is the Fourier transform of $\psi(\vec{r})$. The evaluation of the Laplacian in the momentum space is superior to the finite difference approximation, as it is exact for all plane waves representable by the grid. By applying the operator splitting, the kinetic and the potential propagation are separated, which allows one to choose the optimal space for the both operators: the momentum space for the kinetic operator and the spatial space for the potential. The operator splitted formal solution, Eq. (4.10), can be used in its exponential form and the Fourier transform is used to switch between the momentum and the spatial representations:

$$\begin{aligned}
\tilde{\psi}^{(1)}(\vec{k}, t + \Delta t) &= \exp[-i\hat{T}\Delta t/2\hbar]\tilde{\psi}(\vec{k}, t) \\
\psi^{(1)}(\vec{r}, t + \Delta t) &= \mathcal{F}^{-1}[\tilde{\psi}^{(1)}(\vec{k}, t + \Delta t)] \\
\psi^{(2)}(\vec{r}, t + \Delta t) &= \exp[-i\hat{V}\Delta t/\hbar]\psi^{(1)}(\vec{r}, t + \Delta t) \\
\tilde{\psi}^{(2)}(\vec{k}, t + \Delta t) &= \mathcal{F}[\psi^{(2)}(\vec{r}, t + \Delta t)] \\
\tilde{\psi}(\vec{k}, t + \Delta t) &= \exp[-i\hat{T}\Delta t/2\hbar]\tilde{\psi}^{(2)}(\vec{k}, t + \Delta t)\,.
\end{aligned} \tag{4.16}$$

Again the semi-implicit propagation can be used for the potential term when necessary.

A few remarks which be made. The exponential form is only reasonable for diagonal matrices, because a diagonal matrix remains diagonal in exponentiation, in contrast to any non-diagonal matrix, which would be filled in. In the case of a diagonal operator, the exponential propagators are exact, but even in a nearly diagonal case the improvement can be significant, as the off-diagonal elements are small. Moreover, even though the individual propagators may be exact, the total propagator is still second-order accurate in time, because of the operator splitting. Note that even though a single step has $\mathcal{O}(\Delta t^3)$ accuracy, the repeated application reduces the total order by one to $\mathcal{O}(\Delta t^2)$, and thus the propagator is called second-order accurate. The computational cost is not significantly increased as the Fourier transforms and inverse Fourier transforms can be performed with $\mathcal{O}(N^3 \log N)$ operations by the fast Fourier transform (FFT) technique. In fact, the fast Fourier transforms can be performed using a highly optimized numerical library, which was found to be somewhat faster than the author's implementation of the Crank–Nicolson scheme.

4.1.4 Non-local potential

Computationally the most intensive part of the propagation is the evaluation of the non-local potential. Typically, the potential includes local parts, for example, an external potential, and convolutions, for example, finite (or infinite) range pair-potential. The local parts are clearly easy to evaluate since they lie on the diagonal of the potential matrix. The convolutions are more complicated as they are non-local in the spatial space and would require a total of $\mathcal{O}(N^6)$ operations, if evaluated as three dimensional integrals over

N^3 points for each N^3 points of the grid

$$[\rho * U](x, y, z) = \iiint \rho(x', y', z') U(|x - x'|, |y - y'|, |z - z'|)\, dx'\, dy'\, dz'. \tag{4.17}$$

Fortunately, the convolutions are local products in the momentum space

$$[\rho * U](k_x, k_y, k_z) = \tilde{\rho}(k_x, k_y, k_z) \tilde{U}(k_x, k_y, k_z), \tag{4.18}$$

and again, the Fourier transform can be used to transform the functions to the momentum space, and the inverse transform to transform the convolution back to the spatial space:

$$\begin{aligned} \tilde{\rho}(\vec{k}) &= \mathcal{F}[\rho(\vec{r})] \\ \tilde{U}(\vec{k}) &= \mathcal{F}[U(\vec{r})] \\ [\rho * U](\vec{r}) &= \mathcal{F}^{-1}[\tilde{\rho}(\vec{k}) \tilde{U}(\vec{k})]. \end{aligned} \tag{4.19}$$

This reduces the computational cost from $\mathcal{O}(N^6)$ to $\mathcal{O}(N^3 \log N)$.

The Fourier transform implies periodic boundary conditions, which are not required by the finite difference approximation. In periodic systems, this is clearly an advantage, whereas in non-periodic systems the simulation box must be taken sufficiently large and some potentials might need a cut-off to avoid unphysical periodic effects.

4.1.5 Linearly weighted average

If the potential terms are evaluated only at the grid points, all parts of the potential must be smooth, or otherwise the results can depend strongly on a small change in the grid. For example, if the potential is extremely repulsive within a very short range but slightly attractive elsewhere, an improper choice of the grid could make the potential totally attractive (Figure 4.1). One way to fix this problem could be to take an average of the potential inside a grid cell. However, this can still produce an apparent dependence on a small change, when a sharp feature is near the edge of a grid cell (Figure 4.1). In order to map a function on a grid in such a way that it is not sensitive to small changes, a linearly weighted average of a function can be taken

$$\hat{f}(x) = \frac{\int_{x-\Delta}^{x+\Delta} f(x') w(|x - x'|, \Delta)\, dx'}{\int_{x-\Delta}^{x+\Delta} w(|x - x'|, \Delta)\, dx'} \tag{4.20}$$

where

$$w(|x - x'|, \Delta) = 1 - \frac{|x - x'|}{\Delta} \tag{4.21}$$

and Δ is the grid spacing. The linearly weighted average provides a smooth transition from a grid to another (Figure 4.1), while the characteristics of the function remain and a smooth function is not significantly altered in the averaging. The method also provides better accuracy for convolution integrals than the cell averaging, when the density varies smoothly (as it should for accurate results).

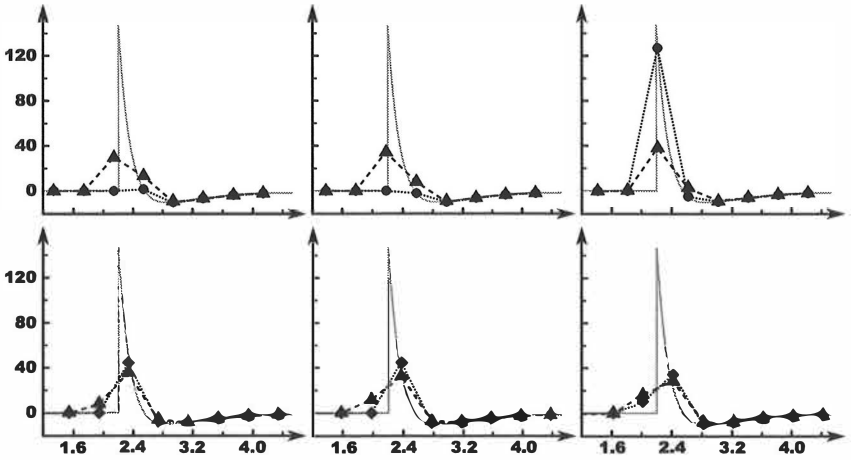

Figure 4.1: The effect of small changes in the grid, when the screened Lennard–Jones pair-potential of the Orsay–Trento functional is sampled in different ways. Circles, no averaging; diamonds, cell averaging; triangles, linearly weighted average; Dashed and dotted lines, guides to the eye.

The linearly weighted average was originally required for the convolution terms in the Orsay–Trento potential. For example, the screened Lennard-Jones pair-potential has a very sharp, repulsive feature near the screening distance, but when it is convoluted with a smooth density, the result is a smooth potential. The idea was to "move" the smoothness of the density to the pair-potential by assuming the density to be linear between the grid points, and then transferring the linear interpolation from the density to the pair-potential:

$$
\begin{aligned}
&\int_{x_i}^{x_i+1} V_l(|x-x'|)\rho_{lin}(x')\,dx' \\
&\to \int_{x_i}^{x_i+1} V_l(|x-x'|)\left[\left(1-\frac{x'-x_i}{\Delta}\right)\rho(x_i)+\left(1-\frac{x_{i+1}-x'}{\Delta}\right)\rho(x_{i+1})\right]dx' \\
&\Rightarrow \rho(x_i)\int_{x_i}^{x_i+1} V_l(|x-x'|)\left(1-\frac{x'-x_i}{\Delta}\right)dx' \\
&\qquad + \rho(x_{i+1})\int_{x_i}^{x_i+1} V_l(|x-x'|)\left(1-\frac{x_{i+1}-x'}{\Delta}\right)dx',
\end{aligned}
\tag{4.22}
$$

which leads to the linearly weighted average of the pair-potential.

The integrals required for averaging in (4.20) must, in general, be performed numerically. The integration can be carried out using a constant number of quadrature points for each grid point; however, in the most cases, the function is mostly smooth and has only one or a few sharp features. If a constant number of points would be used, the accurate integration of the sharp feature requires a large number of points, whereas elsewhere a smaller number of points is sufficient, and thus a large amount of computation time is wasted. However, a simple adaptive integration can save considerable amount of time, especially in a three dimensional case. First, two sets of quadrature points are chosen: a set with a minimum number of points per axis, n_{min}, and another set with $(n_{min}+1)$ points per axis. Then the linearly weighted integral for each grid point is evaluated for the both sets, and as the sets have no common points, and have different weights and step-sizes, it is very probable that the numerical results differ when the integral is not well approximated by the current quadrature points. When the integrals differ, the number of points is doubled at this grid point and the integrals are re-evaluated, until the difference is below the given threshold. The saving of computation time can be significant; for example, if in a three-dimensional case a sharp feature needs 16 points per axis and elsewhere only 4 points per axis are required, the computational effort is reduced by approximately a factor of $(16/4)^3 = 64$. The numerical integration is computationally very demanding, but usually it needs to be done only once in the beginning, as the linearly weighted averages are required from functions which are not changed during the iteration.

4.1.6 Parallel execution

The current implementation of the code can be executed in parallel on symmetric multiprocessing (SMP) computers. The fast Fourier transforms are calculated using a threaded version of the FFTW 2.1.5 library [49]. All other multidimensional loops over the grid are parallelized through the OpenMP 1.0 application program interface [50]. A multidimensional loop has the outermost, middle and innermost loops:

```
for each x
    for each y
        for each z
            grid(x,y,z) = ...
```

Originally, the outermost loop was split into parallel tasks each containing one pass through the middle loop, but the tasks were not of suitable size for an optimal load balancing. To increase the computational efficiency, the outermost and middle loops were combined into one large loop, which was then split into parallel tasks each containing one pass through the innermost loop. Typically, this reduces the size of a parallel task by a few orders of magnitude, *e.g.*, by a factor of hundred.

The smaller tasks alone do not lead to the desired increase of the parallel efficiency, but these have to be combined with a dynamic load balancing. The dynamic load balancing assigns a set of parallel tasks to each processor, and as soon as a processor finishes the current set, a new set of tasks is assigned until none are left. Initially, the sets are large, but become smaller as the number of unassigned tasks is reduced; for example, the set sizes might be 10,9,5,4,2,1 and 1.

4.2 Time-independent density functional theory – imaginary time propagation

The time-dependent Schrödinger (or Kohn–Sham) equation allows one to solve the corresponding time-independent equation [51]. The key idea is to use the imaginary time τ instead of the real time t, which transforms the time-dependent Schrödinger equation into a diffusion equation (kinetic energy) with source and sink terms (potential energy)

$$i\hbar\frac{\partial\psi(t)}{\partial t}=\hat{H}\psi(t)\quad\overset{t\to -i\tau}{\Longrightarrow}\quad -\hbar\frac{\partial\psi(\tau)}{\partial\tau}=\hat{H}\psi(\tau). \tag{4.23}$$

This is in fact similar to what is done in the diffusion Monte Carlo. If the wavefunction $\psi(\tau)$ is expanded as a function of the eigenstates ϕ_i, it is easy to see that all excited states decay faster than the ground state

$$\psi(\tau)=\sum_{i=0}\phi_i e^{-E_i\tau/\hbar}=e^{-E_0\tau/\hbar}\left(\phi_0+\sum_{i=1}\phi_i e^{-(E_i-E_0)\tau/\hbar}\right). \tag{4.24}$$

The same propagators as in the previous section with the real time, *e.g.* the Crank–Nicolson or the exponential propagators, can be used to obtain the ground state. The first excited state is obtained by forcing it to be orthogonal with respect to the ground state. The following excited states are then orthogonalized with respect to all states equal to or below it in energy.

The solution process begins by orthonormalizing the initial guesses, which can be, for example, random vectors. Then the orthonormalized wavefunctions are propagated over one imaginary time step and orthonormalized again. This propagation–orthonormalization procedure is repeated until a convergence is obtained. The orthonormalization can be done using Gram–Schmidt orthogonalization or by calculating the overlap matrix, diagonalizing it and then transforming the non-orthogonal wavefunctions by the eigenvectors of the overlap matrix to orthonormal ones. In practice, the diagonalization of the overlap matrix was found to be more accurate.

In the imaginary time method, the time propagation can be made more efficient by ignoring the semi-implicit propagation and using a higher order operator splitting. The semi-implicit propagation is not necessary as the correct time propagation is not required and, for the last step, when the wavefunctions are converged, the Hamiltonian does not change and thus the propagation is already implicit. The operator splitting, in principle, can be done up to an arbitrary order by taking a proper combination of the exponential propagators

$$e^{\alpha\hat{T}\Delta\tau/\hbar}e^{\beta\hat{V}\Delta\tau/\hbar}e^{\gamma\hat{T}\Delta\tau/\hbar}\cdots e^{\gamma\hat{T}\Delta\tau/\hbar}e^{\beta\hat{V}\Delta\tau/\hbar}e^{\alpha\hat{T}\Delta\tau/\hbar}+\mathcal{O}(\Delta\tau^{\alpha}). \tag{4.25}$$

The problem is that some of the coefficient $\alpha,\beta,\gamma,\ldots$ becomes positive, which causes an unstable propagation for finite imaginary time steps. Fortunately, a fourth-order propagator, which has all coefficients negative, can be formed by including an additional exponential propagator with the commutator

$$[\hat{V}, [\hat{T}, \hat{V}]] = \frac{\hbar}{m} |\nabla V|^2 \tag{4.26}$$

in it [52]. There are several forms for the total propagator, of which

$$e^{-\frac{1}{6}\hat{V}\Delta\tau/\hbar} e^{-\frac{1}{2}\hat{T}\Delta\tau/\hbar} e^{-\frac{2}{3}\left(\hat{V}+\frac{1}{48}[\hat{V},[\hat{T},\hat{V}]]\Delta\tau^2\right)\Delta\tau/\hbar} e^{-\frac{1}{2}\hat{T}\Delta\tau/\hbar} e^{-\frac{1}{6}\hat{V}\Delta\tau/\hbar} \tag{4.27}$$

is used in the most recent code.

The accuracy of the converged solution depends on two things: the selection of the propagator and the time step. The fourth-order propagators are computationally more expensive per iteration than the second-order propagators, but they are more accurate, allowing the use of longer time steps and thus fewer iterations to reach the converged solution with comparable accuracy. When the time step is reduced to one half, the error of the second-order propagator reduces to $(\frac{1}{2})^2 = \frac{1}{4}$, whereas the error of fourth-order propagator reduces to $(\frac{1}{2})^4 = \frac{1}{16}$. If only the accuracy of the converged result is considered, the optimal time step would be infinitely small, but this would require infinitely many iterations to obtain the convergence. On the other hand, the fastest convergence is obtained with a large time step, which is still small enough to avoid the oscillation of the result. Thus, a balance between the convergence speed and accuracy of the result must be found. Again, an adaptive algorithm was found to be an effective and robust way to adjust the time step during the iteration procedure.

The adaptive time step adjustment uses two measures to decide whether to use a shorter time step or not: the total energy of the system and the uncertainty of the energy. To reduce the time step, both measures must be smaller for a shorter time step than for the current one; this assures that the longer time step is used as long as possible. The condition involving the lower total energy is clear: If the longer time step yields a lower energy, there is no reason to reduce the time step. This requirement alone is sufficient for linear systems, but it was found insufficient for nonlinear systems, in which the energy does not necessarily decrease monotonically as the ground state is approached. Thus the uncertainty of the total energy

$$\Delta E = \sqrt{\langle\psi|H^2|\psi\rangle - (\langle\psi|H|\psi\rangle)^2} \tag{4.28}$$

is required to be smaller; this prevents a reduction of the time step when that would increase the variance of the energy. The variance of the energy is zero for the exact solution and an increasing variance thus indicates a worse solution. Together the requirements prefer longer time steps. This is reasonable as a few extra iterations with longer time steps are not very expensive compared to a premature reduction of the time step, which leads to a catastrophic slowdown of the convergence. Note that $\langle\psi|H^2|\psi\rangle$ can be calculated by applying the Hamiltonian once to both sides rather than applying the square of it to only one side.

In order to decide whether the time step needs to be reduced or not, two separate propagations are made on each iteration using two different time steps: the "current" time step $\Delta\tau$ and a shorter time step $\chi\Delta\tau$. If the shorter time step satisfies the required conditions, the shorter time step and the corresponding wavefunctions are used in the next iteration as the "current" time step and wavefunctions. Otherwise, the propagation with the shorter time step is ignored. The adaptive time step adjustment requires twice more effort per iteration than propagation with a constant time step, but the nearly optimal time step for each iteration outweighs the additional computational effort.

The reduction factor χ can be chosen to be a constant between zero and one; however, an adaptive procedure is again more efficient because the optimal factor changes as the iteration proceeds. In the current implementation, the adaptivity is obtained by squaring the factor χ and thus reducing it further when the shorter time step was accepted, or by making the factor χ larger by replacing it with its square root if the time step was not changed. In other words, if the time step was reduced in the last iteration, an even larger reduction is tried on the next iteration, and if it was not reduced, then the reduction was probably too large and a smaller reduction is tried. In practice, there should be upper and lower bounds for the factor χ, for example, $0.1 \leq \chi \leq 0.9$.

The convergence properties depend also on the eigenvalue spectrum of the system. All energies must be above zero; otherwise the propagation becomes unstable as the eigenstates tend to grow rather than decay. Clusters of eigenvalues must be included or excluded as a whole into or out of the set of propagated wavefunctions, because the decay of the error depends on the separation between the states of interest and the rest of the spectrum. The error decays on every iteration by a factor of

$$\frac{e^{-E_{k+1}\Delta\tau}}{e^{-E_k\Delta\tau}} = e^{-\Delta E\Delta\tau}, \tag{4.29}$$

where k is the index for the highest state of interest and $k+1$ is for the lowest state in the rest of the spectrum. If the states corresponding to k and $k+1$ belong to the same cluster, the convergence becomes extremely slow as the energy difference ΔE is close to zero and thus the decay factor $e^{-\Delta E \Delta \tau}$ approaches unity.

To decide when the convergence is reached, one needs a well-defined convergence criterion. If the cluster sizes and the spacings of the eigenvalues are unknown, the upper bound of the error [53] must be used as the convergence criterion:

$$\sqrt{2}\Delta E = \sqrt{2}\sqrt{\langle\psi|H^2|\psi\rangle - (\langle\psi|H|\psi\rangle)^2} \leq \Delta E_{th}, \tag{4.30}$$

where ΔE_{th} is the threshold of the error.

In practice, if the eigenvalue clusters are well separated, after few iterations all states other than the states of interest have decayed and the criterion in Eq. (4.30) is unnecessarily tight. Only the few lowest states in the rest of the spectrum still have a small contribution to the propagated wavefunctions, while the higher states have completely decayed. If upper bounds for the cluster size g_{max} and the minimum spacing ΔE_{min} of the relevant eigenvalue clusters, *i.e.*, those of interest and the next few above, are known, it should be sufficient to require that

$$g_{max} \frac{\langle\psi|H^2|\psi\rangle - (\langle\psi|H|\psi\rangle)^2}{\Delta E_{min}} \leq \Delta E_{th}. \tag{4.31}$$

Clearly, if the eigenvalues are not well separated, *i.e.*, the spectrum is nearly continuous, the minimum spacing ΔE_{min} is very small and/or the maximum cluster size is very large, the upper bound of the error, Eq. (4.30), should be used as the convergence criterion.

Finally, it is interesting to express the imaginary time propagation in terms of the matrix algebra. The imaginary time propagation is equal to the orthogonal iteration for the matrix $\exp(-H\Delta\tau/\hbar)$, or for its operator splitted approximation, if the operator splitting is exploited. The imaginary time propagation requires only $\mathcal{O}(N^3 \log N)$ operations to solve the eigenproblem, whereas, for example, the Lanczos method for Schrödinger equation requires $\mathcal{O}(N^4 \log N)$ operations [48]. The disadvantage of the imaginary time propagation is that only a small number of states can be solved because the computational effort increases as the square of the number of states M, *i.e.*, $\mathcal{O}(M^2)$. However, this could be possibly improved by combining the Lanczos method with the imaginary time propagation.

4.3 Quantum Monte Carlo

The implementation of the quantum Monte Carlo method is quite standard and based on codes presented in [47]. Both the variational and diffusion Monte Carlo implementations are guided, *i.e.*, importance sampled, and the configurations are changed and accepted by one particle at a time rather than all particles together, which increases the acceptance probability and thus the "mobility" of the particles in the configuration space. The trial wavefunction is a product of one- and two-body wavefunctions

$$\psi_T(\vec{r}_1, \vec{r}_2, ..., \vec{r}_n) = \Pi_i \phi_i(\vec{r}_i) \Pi_{j>i} \phi_{ij}(|\vec{r}_i - \vec{r}_j|) \tag{4.32}$$

and does not have to be normalized. The wavefunction, and the analytic gradients and Laplacians of each one- and two-body wavefunctions must be supplied by the user.

The trial energy E_T is adjusted in the diffusion Monte Carlo in order to keep the number of walkers reasonable. If it is not adjusted, or is adjusted too slowly, the number of walkers will either blow up or go to zero. On the other hand, if it is adjusted too tightly, it will bias the distributions and thus also the expectation values. To obtain a reasonable guess for the trial energy and the walker positions, a variational Monte Carlo run is carried out before the diffusion Monte Carlo. Then the diffusion Monte Carlo iteration just continues the VMC iteration and the trial energy is adjusted for each iteration to keep the number of walkers N_{cur} near the preferred one N_{pref} by

$$E_{iter} = E_T - \kappa \ln \frac{N_{cur}}{N_{pref}}. \tag{4.33}$$

If the number of walkers is below the preferred value, the trial energy for the next iteration E_{iter} is increased and more likely the number of walkers will increase on the next iteration. In the opposite case, the trial energy E_{iter} is decreased and the walkers are more likely to die. Initially, the factor κ should be large and the trial energy for iteration depends strongly on the number of walkers. As the iteration proceeds the energy expectation value improves. After the user-defined number of iterations, the new energy expectation value is set as a goal trial energy E_g and the current trial energy E_T is smoothly changed to the goal trial energy during the following iterations. At the same time, the factor κ can be reduced in order to obtain a smaller bias. This trial energy adjustment is done on each user-defined iteration; it allows one to start with a bad guess for the trial energy while still avoiding a large bias in the final result.

The variational Monte Carlo is trivially parallelized by sharing the walkers equally between processors, whereas the diffusion Monte Carlo requires some load balancing. This is done by first gathering the number of walkers on each processor, then sorting the processors in a decreasing order respect to the current number of walkers, and finally balancing the load by moving a required number of walkers from a processor to the next one.

Chapter 5

Results and discussion

In this chapter three different systems are examined to demonstrate the diversity of problems solvable by the methods described in the previous chapters. The first system consists of molecular hydrogen dissolved in superfluid ^{4}He, where the solvation of triplet Rydberg states is explored using the bosonic density functional theory and the hybrid DFT–DMC method. The second system represents the time-dependent case, where a solvated chemical impurity is excited from an electronic state to another with a different symmetry. The spectrum is calculated from the time-evolution of the superfluid rather than from the linear-response theory. In the third system, the electronic and bosonic density functional methods are combined to explore the solvation of excess electrons in superfluid ^{4}He.

5.1 Solvation of triplet Rydberg states of molecular hydrogen in superfluid ^{4}He

Solvation of molecular impurities in superfluid helium has been studied in both helium droplets and bulk helium [17]. From the experimental point of view, the approach based on droplets has been more successful in introducing chemical impurities into liquid helium for spectroscopic studies. The experiments with bulk superfluid suffer from very limited solubility and rapid clustering. Only a few molecules, H_2, He_2^*, O_2, N_2, metal dimers and trimers, have been observed experimentally in bulk superfluid [17, 18], and of these O_2 and N_2 were found to be clustered rather than isolated monomers [54]. Despite its problems, bulk superfluid is the more desirable medium for many experiments, as it has wider accessible temperature and pressure ranges than the droplets and there are no boundary effects in the bulk.

Experimentally He_2^* is a special case which can be created by bombarding the liquid by highly energetic particles [55] or by using strong laser field ionization [56]. As a result of intrinsic excitations, metastable He_2^* triplet excimers are formed. The metal dimers and trimers can be produced by laser ablation of a solid metal target embedded in the liquid [57]. After diffusion the ablated atoms recombine to dimers and trimers. A similar procedure can be applied to produce metastable H_2^* triplet excimers [18]. A solid hydrogen target is embedded into the liquid and is then irradiated by a proton beam. The proton beam excites ground state molecules to triplet excimers, which are ejected into the surrounding liquid. In the He_2^* experiments, as well as in the metal dimer and trimer experiments, both the absorption and emission spectra were measured, whereas in the H_2^* experiments only the emission spectrum was recorded as it is easier to measure. However, in general emission is not as strongly coupled to the surrounding helium bath as absorption, because usually the electronic wavefunctions are contracted in emission, whereas they are expanded in absorption. An expanding wavefunction must do work against the surrounding liquid, which leads to a stronger coupling. In paper I, theoretical calculations were carried out to predict the emission and absorption spectra of the H_2^* triplet Rydberg states solvated in superfluid. The formation of possible H_2^* - $n\mathrm{He}$ complexes was also discussed.

In the gas phase, the first four triplet states of H_2^* are labeled as $b^3\Sigma_u^+$ $(1s\sigma_g\ 1s\sigma_u)$, $c^3\Pi_u$ $(1s\sigma_g\ 2p\pi_u)$, $a^3\Sigma_g^+$ $(1s\sigma_g\ 2s\sigma_g)$ and $e^3\Sigma_u^+$ $(1s\sigma_g\ 2s\sigma_u)$. The states c, a, and d are Rydberg states and correspond to the $2s^1 + 2p^1$ asymptotes. Based on the *ab initio* ICMRCI/d-aug-cc-pV6Z (internally contracted multireference configuration interaction with doubly augmented, correlation consistent, polarized V6Z basis) calculations, it can be seen that the Rydberg states are bound, whereas the b state is dissociative producing two ground state hydrogen atoms (Figure 5.1). The transitions $e \longrightarrow a$ and $a \longrightarrow b$ are dipole allowed and provide a decay channel for the e and a states. The radiative lifetime of 30.2 ns for the e state was obtained using the Fermi golden rule, and the required Frank–Condon factors were integrated from numerically solved vibrational wavefunctions of the e and a states. The c state is metastable as the transition $c \longrightarrow b$ is forbidden.

The shapes of the Rydberg orbitals are shown in Figure 5.2 and can be used to qualitatively describe the interaction between a helium atom and the excimer. The ionic H_2^+ core attracts the helium atom, but the Pauli repulsion

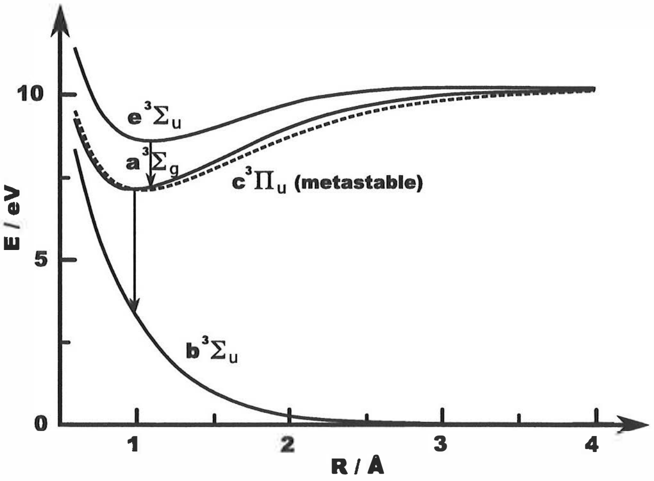

Figure 5.1: Potential energy curves for the first four triplet states of H_2^*.

between the Rydberg electron and the closed shell helium atom causes strong repulsion wherever there exists a significant Rydberg electron density. As a result, the interaction is attractive mainly on the nodal planes and repulsive elsewhere. The calculated H_2^*–He potential energy curves (Figure 5.3) verify the qualitative analysis. The potential energy surface calculations were performed in two geometries: collinear (L) and perpendicular (T) with respect to the molecular axis of H_2^*. The interatomic separation of H_2^* was kept fixed and was chosen to be 1.047 Å, the average of the e and a equilibrium distances, whereas the H_2^*–He distance was varied. Because the DFT and DMC calculations involve many helium atoms, the interaction between the excimer and a helium atom should be pairwise additive in order to be usable for these calculations. To test this, an additional helium atom was placed symmetrically with respect to the other. The calculations were repeated and it was verified that the interaction is pairwise additive as the three and four-atom calculations produced essentially the same H_2^*–He potential energy curves. It was also verified that the ionic core (H_2^+) does not break if the helium atom approaches at close distances.

In order to model the solvation structures of the excimers in bulk superfluid helium, the bosonic density functional theory with the Orsay–Paris [44] or the Orsay–Trento functional [46] was used for helium. For the e and a states, the excimer was assumed to rotate freely, which averages the H_2^*–He interaction to spherical symmetry (Figure 5.3c). In the experiments a rotational structure was observed from several vibronic bands. The functionals

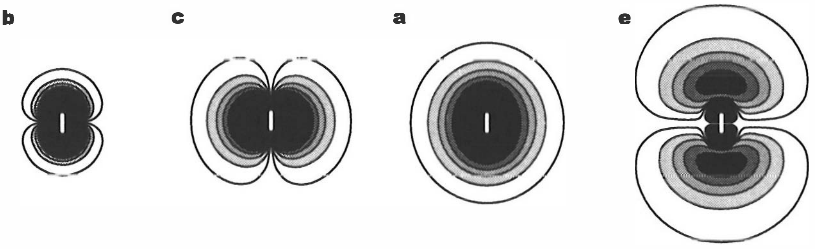

Figure 5.2: Orbital (HOMO) isosurfaces for the first four triplet states of H_2^*.

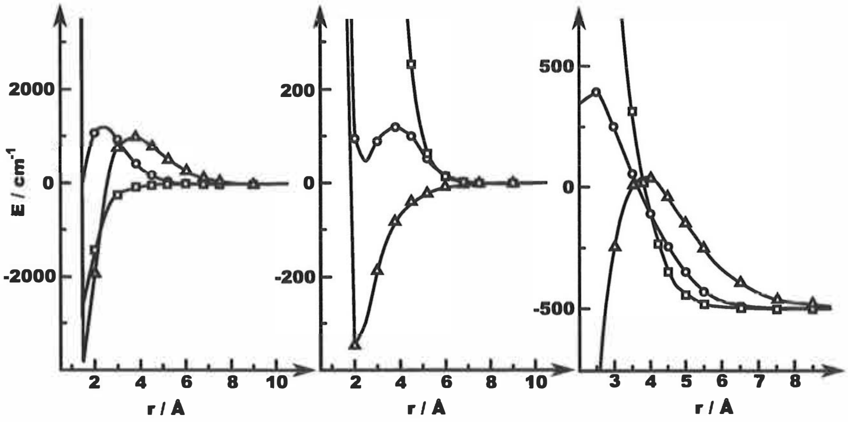

Figure 5.3: Potential energy curves for H_2^*–He a) in collinear (L) and b) in perpendicular geometries, and c) the spherical averages of H_2^*–He potentials. Circles, *a* state; triangles, *e* state; squares, *c* state.

are restricted to zero temperature but the finite temperature of the experiments, 3.0–4.2 K, was simulated in an approximate way by adjusting the bulk density. The calculations for the freely rotating molecules exploited the spherical symmetry reducing the system to a one-dimensional problem, and the helium wavefunctions were optimized in a self-consistent way using the ARPACK eigenproblem library [58]. The helium density profiles (Figure 5.4) were found to be essentially unchanged in the temperature range 0–2 K, *i.e.*, below the λ-point, as the bulk density remains nearly constant. Above the λ-point, the bubble edge is moving further away from the excimer and it becomes more diffuse. This allows the electronic system to behave more like that in the gas phase, which can be seen in the emission ($^3e \rightarrow {}^3a$) and absorption ($^3e \leftarrow {}^3a$) spectra (Figure 5.5) as the blue shift and linewidth are reduced closer to the gas phase values at higher temperatures. By comparing the spectra, it can be seen that the absorption line is an order of magnitude more blue-shifted than the emission line and the linewidth is also much broader. The electronic spectra were simulated by an approximate expression of Anderson [59–61], which requires only the initial helium density $\rho_{He}(\vec{r}, 0)$ and the external potential of helium in the initial and final states $V_i(\vec{r})$ and $V_f(\vec{r})$, respectively:

$$I(\omega) \approx \int c(t) e^{i\omega t}\, dt, \tag{5.1}$$

where

$$c(t) = \exp\left\{ -\int \left[1 - e^{-i\left(V_f(\vec{r}) - V_f(\vec{r})\right)t/\hbar} \right] \rho_{He}(\vec{r}, 0)\, d^3r \right\}. \tag{5.2}$$

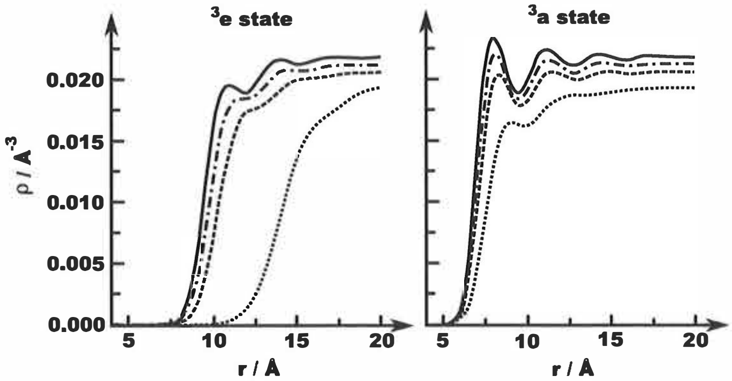

Figure 5.4: Helium density profiles around freely rotating H_2^*–He at different temperatures. Dotted, 4 K; Dashed: 3.4 K, Dot-dashed: 3 K, Solid: 0 K, 1 K and 2 K.

The c state is of special interest as it is metastable and could serve as an intermediate state in absorption experiments. The c state is doubly degenerate in the gas phase and thus the electron density has cylindrical symmetry around the molecular axis, which becomes averaged to spherical symmetry by free rotation. If the c state rotates freely, the solvation structure is otherwise similar to the a state, but the bubble edge is about 0.6 Å closer to the center at zero temperature. However, if the degeneracy is broken and the free rotation is quenched, one of the two degenerate orbitals is energetically favored relative to the other. As a result, the electron might occupy only the favored orbital as the liquid relaxes around it, thus further lowering the energy. In this case, the helium atoms reside in a strongly anisotropic potential, which is attractive near the nodal plane and repulsive elsewhere. To examine the

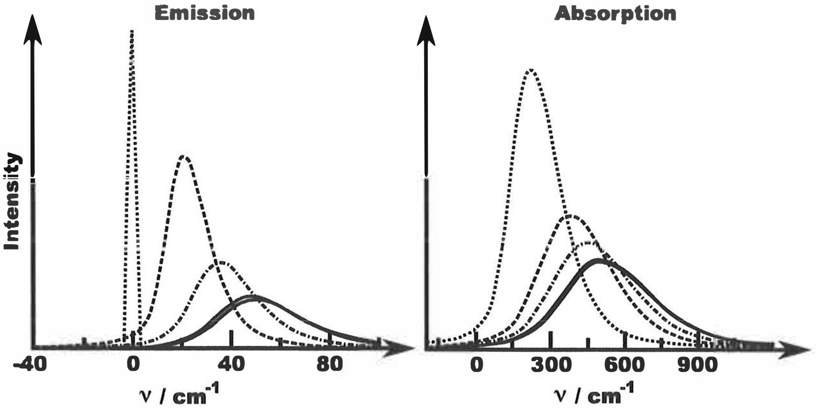

Figure 5.5: Emission ($^3e \rightarrow {}^3a$) and absorption ($^3e \leftarrow {}^3a$) spectra of H_2^* solvated in liquid helium. Dotted, 4 K; Dashed: 3.4 K, Dot-dashed: 3 K, Solid: 0 K, 1 K and 2 K.

solvation structure in this case, the 3D bosonic density functional method was applied, but it was found that the potential is too attractive for the DFT as excessive unphysical densities were found on the nodal plane. Thus the diffusion Monte Carlo method was applied to model the strongly bound part. The DMC calculations, which included the excimer and a few helium atoms, showed that the minimum energy was reached with four helium atoms in the strongly bound region. Beyond four atoms the helium density began to leak to the surrounding region. A very accurate helium–helium pair-potential of Aziz *et al.* [11] was used in the DMC calculation. The density obtained from DMC was convoluted by the pair-potential, and it was used together with the original H_2^*–He potential as the external potential for the DFT calculation. After the DFT calculation, the DMC calculation was repeated including the repulsion from the DFT density. The DMC–DFT cycle was repeated several times to reach convergence for both densities. The resulting highly anisotropic solvation structure is presented in Figure 5.6. The two parts of the systems, the strongly bound (DMC) part and the rest of the system (DFT), can be treated separately, because there is no overlap in the corresponding densities. To summarize, if the breaking of degeneracy and quenching of the rotation would happen, H_2^*–(He)$_n$ complexes may form, and thus the emission and absorption spectra would be heavily influenced by the penetration of the helium into the nodal plane. Otherwise, the c state is energetically slightly favored over the a state by the liquid.

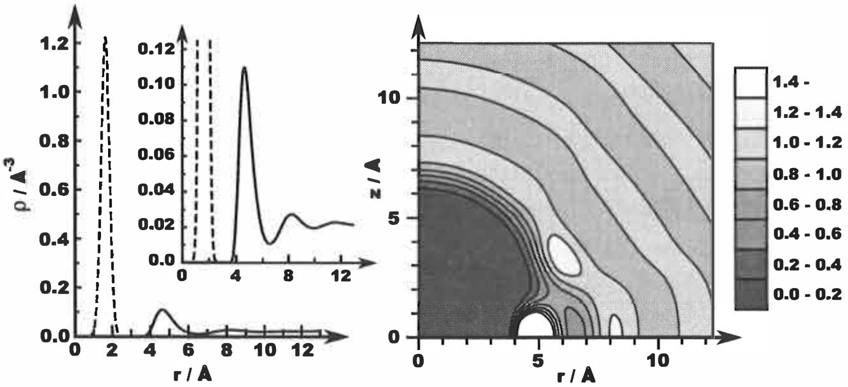

Figure 5.6: Anisotropic solvation structure of ^3c state. Left: The density profile in the nodal plane of the Rydberg orbital. Dotted line, DMC density. Solid line, DFT density. Right: A contour plot of the DFT density perpendicular to the nodal plane. Greyscale, density in units of the bulk density.

5.2 Two-level anisotropic electronic system in superfluid ^{4}He

As discussed in the previous section, electronic spectroscopy of atoms and molecules (chromophores) in superfluid helium has been more successful in helium droplets than in bulk helium. As the chromophores are easily captured by droplets, a wide range of atoms and molecules has been experimentally studied [20]. The experiments show that if the chromophore–liquid interaction is weak enough, the zero phonon line in the linear absorption spectrum is accompanied by a structured phonon sideband. This sideband has been interpreted to interrogate the dynamics of the superfluid around the chromophore during its excitation [62]. Typically, the sideband contains two broad maxima located approximately at 8 and 14 K on the blue side of the zero phonon line. The existence of these maxima has been used as an argument that the droplets are in the superfluid state, as the energies correspond to the energies of the maxon and the roton minimum, which are the turning points of the dispersion relation. At the turning points, density of states is high and the group velocity is zero, which allows the excitations to localize near the chromophores. Thus the coupling of the corresponding modes with the chromophore is stronger.

Theoretical path-integral Monte Carlo calculations support the experimental observations by predicting superfluidity of the droplets [63]. While the path integral Monte Carlo cannot be used to predict the linear absorption spectrum, the density functional theory can. In the previous DFT calculations [61], the chromophore–liquid interaction was assumed to be angularly isotropic, which allows an efficient solution of the problem by taking advantage of the spherical symmetry and solving the problem in 1D. The calculations were found to agree with the experiments and reproduced the two maxima. However, to explore the effect of an anisotropic interaction, the density functional equations must be solved numerically in 3D. This is computationally very expensive. The memory requirement scales cubically as the function of the droplet diameter and exceeds the capabilities of modern supercomputers even for relatively small droplets. Another issue is the time propagation needed for the calculation of the spectrum. The propagation time must be hundreds of picoseconds in order to obtain a good resolution in the spectrum, whereas the time step must be fairly short, only tens of femtoseconds, in order to obtain a good accuracy. This leads to thousands of iterations and thus to long run times even on supercomputers.

In paper III, a hypothetical atom was used as an anisotropic impurity. Four different cases were simulated: 1) anisotropic ground state with isotropic excited state, 2) isotropic ground state with anisotropic excited state, 3) and 4) are spherically averaged (isotropic) versions of 1) and 2), respectively. The first case mimics a boron atom, in which the unpaired electron is on the p_z-orbital, but with a simplified interaction. In the case of the anisotropic ground state, the xy–plane, the nodal plane of the p_z orbital, had a 25 K bound Morse interaction $V_M(\vec{r})$ between the liquid:

$$V_M(r) = D_e \left[\left(1 - e^{-\alpha(r-r_e)}\right)^2 - 1 \right], \tag{5.3}$$

where $D_e = 25$ K, $\alpha = 1.5$ Å and $r_e = 3.5$ Å, and the z–axis had an exponentially decaying and purely repulsive interaction

$$V_R(r) = D_e e^{-2\alpha(r-r_e)}. \tag{5.4}$$

The potential was interpolated into the shape of interaction from a p_z–type orbital:

$$V(r,\theta,\phi) = 2V_{xy}\sin^2\phi + V_z\cos^2\phi. \tag{5.5}$$

The excited state was taken to have the repulsive interaction $V_R(\vec{r})$ in all directions, which resembles the interaction of an s–type orbital. In the second case, the isotropic ground state had the Morse interaction in all directions and the excited state was the same as the anisotropic ground state of the first case. For the third and fourth cases, the anisotropic potential was replaced by an isotropic potential, which is the average of all directions: $V_{iso} = \frac{1}{3}(V_x + V_y + V_z)$.

The chromophore was assumed to have only two well-separated energy levels, the ground and the excited state, and the superfluid was assumed to behave adiabatically with respect to the electronic system. After the electronic excitation the liquid bath begins to evolve. Due to the adiabatic approximation the liquid cannot produce transitions; however, it modulates the electronic energy levels of the chromophore. The modulation of the levels was recorded and transformed to the linear absorption spectrum. The first order polarization

$$P^{(1)}(\omega, t) = \langle \psi^{(0)}(t) | \hat{\mu} | \psi^{(1)}(t) \rangle \tag{5.6}$$

can be used to obtain the linear absorption spectrum by Fourier transforming it to $P^{(1)}(\omega, \omega')$ and setting $\omega = \omega'$. The zeroth and first order electronic wavefunctions are

$$\psi^{(0)}(t) = \exp\left[-\frac{i}{\hbar} \int_0^t H_0(t') dt' \right] \psi^{(0)}(0) + c.c., \tag{5.7}$$

where $H_0(t')$ is the time-dependent electronic Hamiltonian including the bath interaction, and

$$\psi^{(1)}(t) = -\frac{i}{\hbar} \int_0^t \exp\left[-\frac{i}{\hbar} \int_{t'}^t H_0(t'') dt'' \right] H_1(t') \psi^{(0)}(t') dt', \tag{5.8}$$

where $H_1(t') = -\mu\varepsilon(\omega, t')$ corresponds to the interaction between the light and the chromophore, μ is the transition dipole moment and ε is the electric field. After substitution of the wavefunctions, the first order polarization becomes

$$P^{(1)}(\omega, t) \propto i \int_0^t \exp\left[-\frac{i}{\hbar} \int_{t'}^t E_{ext}(t'') dt'' - i\omega t' \right] dt' + c.c., \tag{5.9}$$

where

$$E_{ext}(t) = \int \rho^e_{He}(\vec{r}, t) V_e(\vec{r})\, d^3r - \int \rho^g_{He}(\vec{r}) V_g(\vec{r})\, d^3r, \tag{5.10}$$

$\rho^g_{He}(\vec{r})$ and $\rho^e_{He}(\vec{r}, t)$ are the ground and excited state helium densities, respectively, and $V_g(\vec{r})$ and $V_e(\vec{r})$ are the corresponding chromophore–helium pair-potentials. The electronic part was removed as it is only a constant offset in the resonance energy. Finally, the intensity of the linear absorption spectrum is obtained as

$$I(\omega) \propto \left| \mathcal{F} \left[\exp \left(\frac{i}{\hbar} \int_0^t E_{ext}(t')dt' \right) \right] \right|^2 . \tag{5.11}$$

Another possibility is to directly transform the modulation of the energy difference, Eq. (5.10).

The droplet size used in the simulations was 200 helium atoms, and the chromophore was placed in the middle of the droplet. Before the time propagation could be done, the ground state solvation structures had to be found. This was done using the imaginary time propagation combined with the Orsay–Trento functional. The resulting densities are shown in Figure 5.7. The spatial grid consisted of 256×256×256 points with a step size of 0.21 Å (0.4 bohrs). The ground state of the first case with the anisotropic ground state shows significant anisotropy for the liquid. The first solvation layer in the xy–plane has a maximum, which is approximately three times the bulk density, whereas in the repulsive z–direction, the maximum is only slightly above the bulk density. In the corresponding isotropic case, the third case, the maximum is twice the bulk density. The second case with the anisotropic excited state and the corresponding isotropic case have the same isotropic ground state with the first layer maximum of two and half times the bulk density.

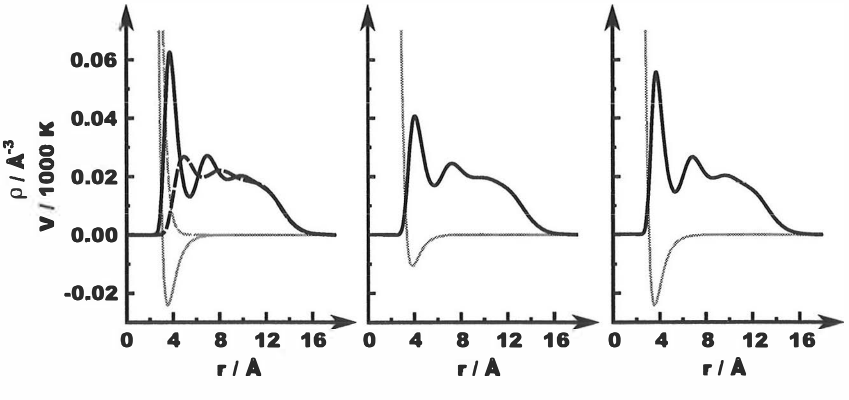

Figure 5.7: Ground state helium densities (black) and potential (grey). Left: Anisotropic ground state (case 1). Middle: Spherically averaged anisotropic ground state (case 3). Right: Isotropic ground state (cases 2 and 4). Solid line, xy-plane; dashed, z-plane.

The real-time propagation used the semi–implicit Crank–Nicolson propagator and the Orsay–Trento functional with backflow terms included. Initially, the helium density was set equal to the ground state density. The electronic excitation was initiated at time zero, and helium was propagated in the excited state potential. The dynamics were then followed for the total simulation time of 140 ps with a time step of 10 fs. An imaginary potential was used as absorbing boundaries to prevent any evaporated liquid from entering the outer periodic boundary. Snapshots of the dynamics are shown in Figure 5.8. In the case of anisotropic ground state the initial anisotropy was quickly smoothed out and density waves were left bouncing between the chromophore and the droplet surface. The density waves had slightly higher amplitude in the xy–plane than along the z–axis, as more helium must be relocated from the neck of the p_z-orbital during the excitation. In the corresponding isotropic case there is no anisotropy and the density wave is a spherically symmetric standing-wave mode, S-mode. The frequency of the mode is approximately determined by the distance between the inner (chromophore) and outer (droplet surface) edges of the density as the waves travel at the speed of sound. In the anisotropic excited state, the isotropic solvation structure is quickly transformed to anisotropic one and again, a similar, long-term standing-wave motion occurs.

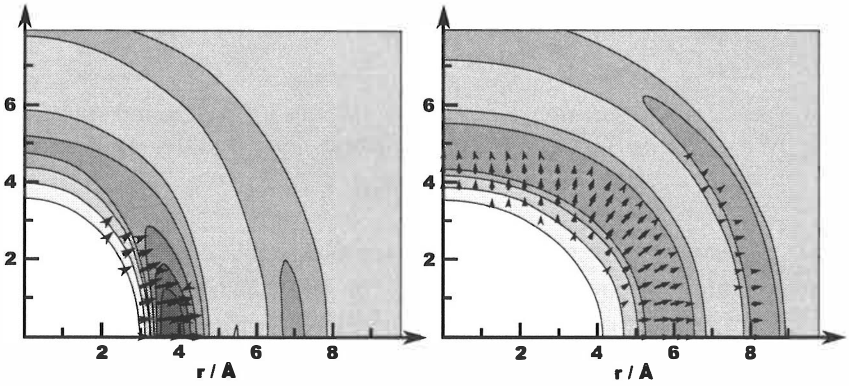

Figure 5.8: Snapshots of the liquid evolution after excitation from anisotropic ground to isotropic excited state (case 1). Left: At time 100 fs. Right: At time 1000 fs. Greyscale contours, density; arrows, momentum ($\rho\vec{v}$).

In both cases, the linear absorption spectra obtained are practically identical for the anisotropic and isotropic systems (Figure 5.9). The only prominent features in the spectra, along with the sharp zero phonon lines, are the standing-wave modes at 3.3 K for the anisotropic ground state and at 3.5 K for the anisotropic excited state. The overtones of the standing-wave motion are not shown because they are above the cut–off energy. The cut-off energy is equal to the single particle binding energy, ~5 K, which is required for evaporation. However, the standing-wave modes are not observed in the experimental spectra, because at above zero temperatures such modes are subject to serious inhomogeneous broadening. If the chromophore is only weakly trapped, as in the present case, the chromophores are not located at the center of droplets, but rather have a distribution which depends on the trapping potential, droplet size, and temperature. Moreover, the size distribution of the droplets causes an additional broadening in the experiments.

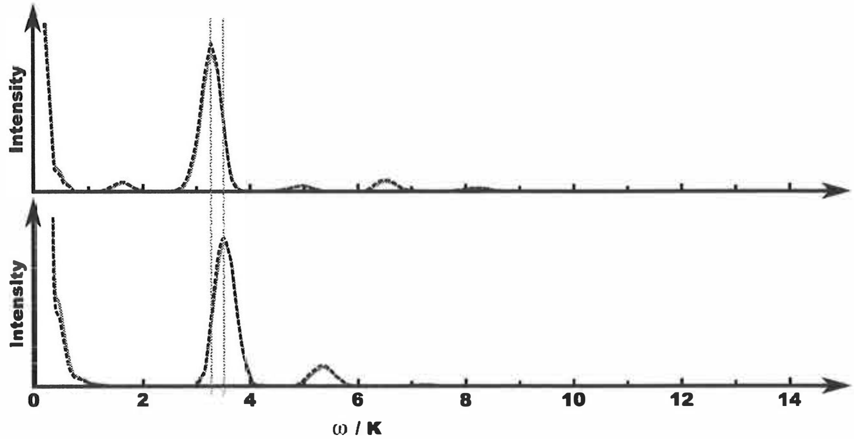

Figure 5.9: Top: Absorption spectrum for the anisotropic ground state. Bottom: Absorption spectrum for the anisotropic excited state. Dashed black line, anisotropic; solid grey line, isotropic.

It was observed that the two methods used to simulate the linear absorption spectrum, the expression (5.11) and the direct Fourier transform of the equation (5.10), did not produce significantly different spectra. The Fourier transform approach was found to give larger intensities at higher energies, which is actually an advantage, because the experiments use high laser intensities. A high laser intensity saturates the zero phonon line and thus enhances the high-energy bands.

To summarize, the anisotropy does not alter the linear absorption spectra for small droplets, and the maxon and the roton minimum are not shown in the spectra, which is probably due to boundary effects. The droplet boundary is too close to the localized excitations, which are disturbed and thus decay quickly. Simulations for larger droplets and for bulk superfluid would possibly provide more interesting results.

5.3 One and two-electron bubbles in superfluid ^{4}He

An excess electron in liquid helium has been the subject of extensive experimental and theoretical studies [22–24, 64–69]. In the experiments, an excess electron is inserted into helium by a discharge tip, or by an $\alpha-$ or β–source immersed in the liquid [22, 23]. The electron can then be dragged by a static electric field in a chosen direction for excitation and detection. The excess electrons can be monitored either by the induced electric current [22], by exploding the bubble [23], or by optical spectroscopy [66]. The bubble can be exploded by applying a negative pressure to the bubble, which is attained by an acoustic wave. Below a critical pressure, the bubble becomes unstable against unlimited expansion, the electron delocalizes to a plane–wave state and the cavity begins to fill with helium. The delocalized electron is then detected by a He–Ne laser: The laser light is scattered by the delocalized electron and the scattered photons are collected by a photomultiplier. The bubbles in different quantum states have different critical pressures, which is used to distinguish them from each other.

The earlier theoretical studies have mainly used the standard bubble model [64] or a spherically symmetric, one dimensional density functional theory [67]. In the standard bubble model, the liquid is treated as a classical bubble and the electron is approximated as a particle in a spherical square-well of a depth of ~1.0 eV. The energy of the liquid is a sum of the classical surface energy, which is the product of the surface tension γ and the surface area A, and the possible volume energy, which is the product of the external pressure P and the volume of the cavity V. The total energy of the system

$$E = E_e + \gamma A + PV \tag{5.12}$$

includes the kinetic energy of the electron E_e, which is $\frac{h^2}{8mR^2}$ for the ground state. The standard bubble model was extended by Maris [70] to include non-spherical geometries by describing the bubble shape using a linear combination of Legendre polynomials of even order

$$R(\theta) = \sum_{L=0,2,\ldots,L_{max}} a_L P_L(\theta). \tag{5.13}$$

Maris *et al.* calculated the shapes and energies of the bubble for several different quantum states as well as the transition energies and radiative lifetimes [68, 71].

Maris also investigated the possibility of two electrons occupying the same bubble [68]. In a two-electron bubble the electrons repel each other and thus cause a greater internal pressure against the bubble wall. The electronic system was treated with a simple diffusion Monte Carlo method. It was found that the spherical singlet bubble is stable with the radius of 34 Å; however, the bubble was unstable against small perturbations and would dissociate to two distinct one-electron bubbles.

The classical treatment of the liquid assumes a step-function for the gas–liquid interface, *i.e.*, the interface is sharp, and the liquid density is zero inside and equal to the bulk density outside the bubble. The penetration of the electron into the liquid is also prevented by the model, and the value of the surface tension, which should be used in microscopic systems, is unclear. To address these problems in paper V, a theoretically more rigorous bosonic density functional theory was used for helium together with an electron–helium pseudopotential of Jortner *et al.* [72]. The Orsay–Trento density functional produces accurately the smooth, finite-width gas–liquid interface and, together with the pseudopotential, it allows the electron to penetrate into the liquid.

The electron and liquid helium form a coupled, non-linear system, for which the time-dependent equations can be written as

$$\begin{aligned} i\hbar\frac{\partial\psi_{He}(\vec{r},t)}{\partial t} &= -\frac{\hbar^2}{2M_{He}}\nabla^2\psi_{He}(\vec{r},t) \\ &\quad + U_{OT}[\psi_{He}]\psi_{He}(\vec{r},t) + \int U_{el-He}(|\vec{r}-\vec{r}_2|)\rho_{el}(\vec{r}_2,t)d^3r_2\,, \end{aligned} \tag{5.14}$$

where $U_{OT}[\psi_{He}]$ is the Orsay–Trento potential, and

$$i\hbar\frac{\partial\psi_{el}(\vec{r},t)}{\partial t} = -\frac{\hbar^2}{2m_{el}}\nabla^2\psi_{el}(\vec{r},t) + \int U_{el-He}(|\vec{r}-\vec{r}_2|)\rho_{He}(\vec{r}_2,t)d^3r_2\,, \tag{5.15}$$

where $U_{el-He}(r)$ is the electron–helium pseudopotential. The states were solved numerically using the imaginary time propagation for both equations simultaneously. On each iteration step, both the electron and helium wavefunctions were propagated once and then the electronic wavefunctions were orthonormalized. It was found more efficient to update the densities as frequently as possible, *i.e.*, on each iteration, rather than waiting until the wavefunctions are converged.

5.3.1 One-electron bubbles

The one-electron bubbles were calculated exploiting the operator splitting together with the exponential propagators in the imaginary time propagation. The grid was chosen to consist of 128×128×128 grid points with 0.8 Å spacing, as essentially the same results were obtained with the considerably more expensive 256×256×256 points and 0.4 Å spacing. The integrals required for linearly weighted averages were evaluated using steps as small as 0.025 Å. The system had periodic boundaries; however, the simulation box was chosen sufficiently large to eliminate the periodic effects.

The solutions were sought for the three lowest states: 1S, 1P and 1D. The ground state of the one-electron bubble is the spherical 1S state (Figure 5.10 and Figure 5.11). If the electron is excited from the ground state to its first excited state 1P, it obeys the Frank–Condon principle, and initially, the helium density remains spherical, whereas the electron wavefunction forms a nodal plane (Figure 5.11). Consequently, the electron density is no longer spherical, leading to an anisotropic external potential for the liquid. Helium adapts to the new potential, which, in turn, breaks the symmetry of the electron's external potential. The anisotropy increases until a balance is reached and the shape resembles a peanut *i.e.*, two slightly overlapping spheres (Figure 5.10). Furthermore, in the equilibrium geometry of the second excited state 1D, the electron wavefunction has two nodal planes in parallel (Figure 5.11) and the shape of the bubble is further elongated to three slightly overlapping spheres on a line instead of two (Figure 5.10).

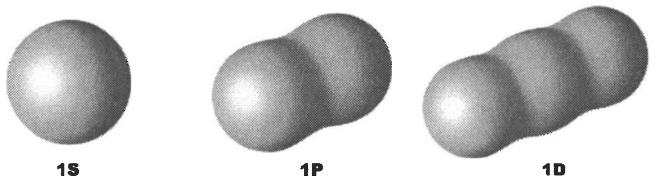

Figure 5.10: Isosurfaces of the helium densities for the first three states of one-electron bubbles.

The energies of the electronic states for different equilibrium geometries are shown in Figure 5.12. A summary of the bubble properties together with the classical approximations for the surface energies are presented in Tables 5.1 and 5.2. The $2R_{\|}$ is the length of the bubble, $2R_{\perp}$ is the width, E_{tot}, E_{el} and E_{He} are the total, electronic and helium energies from the DFT calculation, respectively. The surface area A_{iso} corresponds to $\rho = \frac{1}{2}\rho_{bulk}$

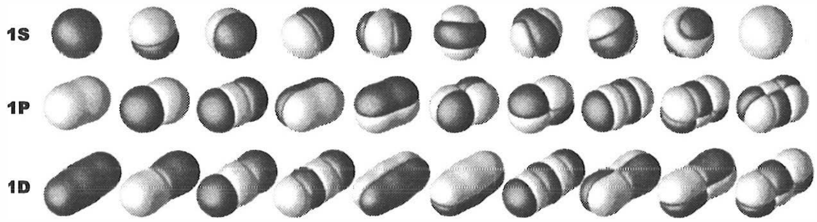

Figure 5.11: Isosurfaces of the first ten electron wavefunctions for the first three states of one-electron bubbles.

helium isosurface. The classical surface energies $\gamma_1 A$ and $\gamma_2 A$ are given for two different surface tensions, $\gamma_1 = 0.247$ K/Å and $\gamma_2 = 0.275$ K/Å, and the effective surface tension is defined as $\gamma_{eff} = E_{He}/A_{iso}$. The transition dipole moments, required for oscillator strengths and radiative lifetimes (Table 5.2), were calculated by a numerical integration of $\langle\psi_{el}^{(i)}|\vec{\mu}|\psi_{el}^{(j)}\rangle$. These results are in reasonable agreement with the results obtained by the classical bubble [68,71].

State	$R_\parallel$ [Å]	$R_\perp$ [Å]	E_{tot} [K]	E_{el} [K]	E_{He} [K]	A_{iso} [Å^2]	$\gamma_1 A$ [K]	$\gamma_2 A$ [K]	γ_{eff} [K/Å^2]
1S	18	18	2110	1026	1084	4003	1101	989	0.2708
1P	28	16	2883	1415	1468	5447	1498	1345	0.2695
1D	37	15	3485	1722	1763	6560	1804	1620	0.2688
∘1P	22	22	3168	1555	1613	5972	1642	1475	0.2701

Table 5.1: Summary of results for the one-electron bubbles. Units are Ångströms and Kelvins. See text for the description of quantities. ∘1P denotes the spherically symmetric 1P state.

Transition	Type	Oscillator strength / Radiative lifetime	ΔE [meV]
1S ⇢ 1P	$\Sigma_g - \Sigma_u$ $\Sigma_g - \Pi$	$f = 0.95$	111
1P ⇢ 1D	$\Sigma_u - \Sigma_g$	$f = 0.61$	75
1P → 1D	$\Sigma_u - \Pi$	$f = 0.64$	135
1P ⇢ 1S	$\Sigma_u - \Sigma_g$	60 μs	35
1D ⇢ 1P	$\Sigma_g - \Sigma_u$	40 μs	31

Table 5.2: Oscillator strengths, transition lifetimes and energies for some transitions of the one-electron bubbles.

The width of the 1P and 1D bubbles is smaller than that of the 1S bubble, which decreases the effective inertia of the bubble and thus the increases the velocity when dragged. Therefore, the 1P and 1D bubbles could explain the

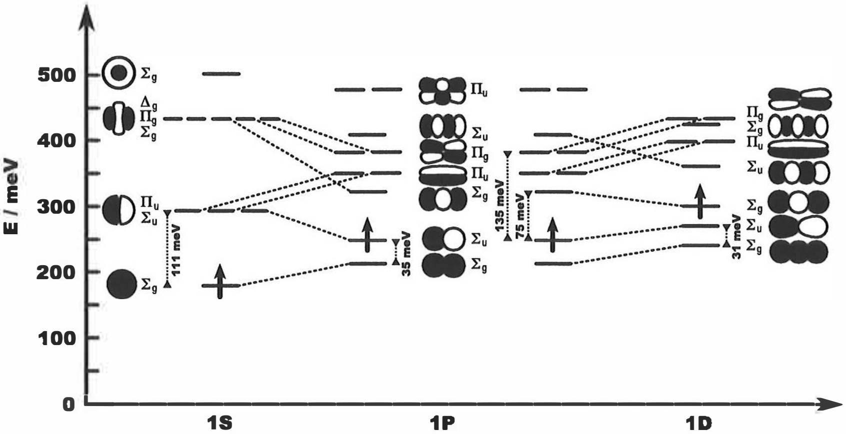

Figure 5.12: Energies of the electronic states for different equilibrium geometries for the one-electron bubbles

exotic (fast) ions, but the radiative lifetimes, 60 μs and 40 μs, (Table 5.2) are too short compared to the timescales of the experiments, ~1 ms [22]. Ghosh and Maris carried out experiments for determining the lifetime of the 1P state and obtained an estimate of 50 ns [73]. As it is significantly shorter than the radiative lifetime, they proposed that some non-radiative process must be responsible for destroying the 1P state. However, in paper V, no plausible non-radiative process was found with a lifetime of the same order as the estimated lifetime of 50 ns. For example, the bubble dynamics leading from 1S to 1P is expected to proceed in the picosecond timescale. Another possibility for explaining the short lifetime is that the 1P state would have two different configurations separated by an energy barrier. In addition to the non-spherical 1P state, a metastable spherically symmetric 1P state, in which the p-orbitals remain degenerate, could exist. However, when the spherical 1P state was propagated in real-time, it began spontaneously to relax towards the non-spherical state.

5.3.2 Two-electron bubbles

When two electrons occupy the same bubble, the electron–electron interaction must be included into the electronic equations:

$$\begin{aligned} i\hbar\frac{\partial\psi_{el}(\vec{r},t)}{\partial t} &= -\frac{\hbar^2}{2m_{el}}\nabla^2\psi_{el}(\vec{r},t) \\ &+ U_{ee}[\rho_{el}]\psi_{el}(\vec{r},t) + \int U_{el-He}(|\vec{r}-\vec{r}_2|)\rho_{He}(\vec{r}_2,t)d^3r_2\,, \end{aligned} \quad (5.16)$$

where $U_{ee}[\rho_{el}]$ is the Kohn-Sham potential. Initially, the restricted Kohn–Sham scheme with the local density approximation (LDA) was employed for the singlet state, but it produced physically inconsistent results as the electron density was localized into many fractions inside the spherical bubble. The source for this behavior was the self-interaction in the functional. To eliminate it, the self-interaction correction (SIC) of Perdew and Zunger [37] was applied, which produced a smooth, spherically symmetric density. However, the restricted Kohn–Sham scheme was found to prevent the splitting of the bubble, because a single Slater–determinant cannot describe two electrons localized inside two different bubbles. Thus, the unrestricted Kohn–Sham method was applied, which is justified by the alternative interpretation of the spin-density functional theory given by Perdew *et al.* [38]. The unrestricted method requires the use of the spin-density functional and thus the local density approximation was replaced with the local spin-density approximation (LSDA). The same SIC–UKS–LSDA method can also be applied to the triplet state.

For the two-electron calculations, the grid had to be enlarged to consist of 320×320×320 points and a cut-off was set for the Coulomb repulsion in order to prevent periodic effects for the electrons. The singlet state was found to be stable in the spherical geometry with the bubble radius of 33 Å (Figure 5.13). However, when a small non-spherical perturbation was applied, the subsequent imaginary time propagation led to the dissociation of the bubble to two one-electron bubbles. The "reaction path" of the dissociation process cannot be determined from the imaginary time propagation, and thus it was not possible to determine whether an energy barrier exists for the splitting. Even a very small barrier could prevent the splitting at low temperatures. Nevertheless, the results obtained for the singlet state are in agreement with the results obtained by Maris [68] using a combination of the diffusion Monte Carlo and the classical bubble model.

The triplet state has not been considered before and it was anticipated that additional stabilization caused by the spin–spin exchange interaction could be achieved. However, the triplet state was found to be even more unstable than the singlet, as no stable geometries were found and the bubble dissociated without any perturbations. Based on these calculations, it can be concluded that neither the singlet nor the triplet states appear to be stable in bulk superfluid ^{4}He.

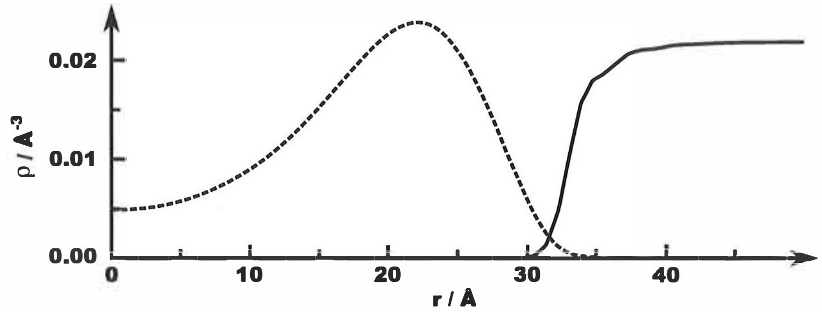

Figure 5.13: The electron and helium densities for the spherical singlet two-electron bubble. Dashed line, electron density multiplied by 1000; Solid line, helium density.

Chapter 6

Summary

Atoms and molecules as well as excess electrons in superfluid ^{4}He can be used to investigate the microscopic properties of an inhomogeneous superfluid. Moreover, superfluid helium offers a homogeneous, ultracold and gentle medium for spectroscopic studies. Experiments have been done in bulk helium and in helium droplets; the droplet approach has been more successful in introducing different species into the liquid. The bulk experiments suffer from a low solubility and rapid clustering of the atoms and molecules. However, the bulk is usually more desirable as it has wider temperature and pressure ranges and it does not suffer from boundary effects. The earlier theoretical studies have mainly used the standard bubble model, the quantum Monte Carlo methods, or the one dimensional, spherically symmetric density functional theory. The standard bubble model uses the classical surface tension and pressure work to describe the bubble; this is not necessarily justified for atomic scale systems. The value of the surface tension to be used is unclear and it is thus regarded as an adjustable parameter. The quantum Monte Carlo methods, for example, the diffusion or path-integral Monte Carlo, are probably the most accurate methods in describing small helium droplets, but they are computationally demanding and thus not suitable for large droplets and bulk superfluid. Moreover, the quantum Monte Carlo methods cannot model (true) time-dependent systems.

In the density functional methods the properties of a system are described by the density alone, at least in principle. As the density is only a function of three variables, the corresponding equations are one-particle Schrödinger equations with effective potentials, and the dimension of the problem does not depend on the number of particles in the system. This is why the density functional theory is especially suitable for large problems with many particles.

The problem is that the exact form of the effective potential is not known and must be approximated. However, accurate functionals have been developed for many different systems, such as superfluid helium or electronic systems in chemistry and solid state physics.

The most advanced functional for the superfluid ^{4}He is the Orsay–Trento functional, which can be used to model both time-dependent and time-independent systems. The functional is a phenomenological functional, in which each term is based on a physical phenomenon, but the coefficients for the terms are determined from the experiments. In the earlier studies, the Orsay–Trento and its predecessors have been used to model bulk superfluid as well as helium droplets and films. In studies where atomic scale impurities have been immersed in helium, the systems have been assumed to be spherically symmetric allowing for an efficient solution in 1-D. However, to study the effect of anisotropy, the systems must be solved fully in three dimensions.

A fully three dimensional system is computationally very demanding and the design of its implementation becomes important. The current implementation developed in this work can be used for both time-dependent and time-independent systems. It utilizes the semi-implicit propagation to accurately handle the non-linearity in the Kohn–Sham equations. The time propagation is accelerated using the operator splitting technique and two different propagators are available: the Crank-Nicolson and the exponential propagators. The non-linear potential includes finite-range interaction in a form of a convolution, which is efficiently evaluated using fast Fourier transforms. The number of grid points can be reduced by taking the linearly weighted averages of the potential terms, *i.e.*, effectively integrating the potential terms with sharp features using greater accuracy than for the rest of the problem. The imaginary time propagation is employed instead of the standard self-consistent field approach to accelerate the convergence of the time-independent problems. Finally, the total execution time was reduced by an efficient parallel execution of loops and fast Fourier transform.

Three different systems were simulated using the methods described in this thesis. In the first system, the first four triplet states of molecular hydrogen dissolved in superfluid ^{4}He were studied. In the case of free rotation, the solvation structures and the related emission and absorption spectra were calculated for several different temperatures using the bosonic density functional theory. At lower temperatures, stronger blue shifts and broader linewidths were observed as the liquid is more dense. The absorption lines were a factor of ten more blue-shifted than the corresponding emission lines. Of the first four triplet states, the c state is of special interest as it is metastable and could be used as an intermediate state for absorption experiments. In the gas phase, the c state is doubly degenerate and the free rotation averages it to a spherical symmetry. However, if the degeneracy of the c state is broken and the free rotation is quenched in the liquid, the helium atoms reside in a highly anisotropic potential. The hybrid DMC–DFT method was applied to the anisotropic system and it was found that H_2^*–$(He)_n$ complexes might form; these would heavily influence the absorption and emission spectra.

In the second case, the effect of anisotropy on the absorption spectrum of small helium droplets was examined. A hypothetical atom with only two well-separated electronic levels was placed in the center of a droplet and excited from the ground state to the excited state. The absorption spectra were calculated from the time-evolution of the system rather than from the linear-response theory. Both the effect of an anisotropic ground state and the effect of an anisotropic excited state were studied and compared to the corresponding isotropic cases. It was found that the absorption spectra of anisotropic and isotropic cases were essentially the same. In all spectra, the only prominent feature in addition to the zero phonon line was the standing-wave mode, which arises from the waves bouncing between the chromophore and the droplet surface. However, this is not seen in the experimental spectra as the impurity is not trapped in the center of the droplet but rather has a distribution which depends on the trapping potential, droplet size and temperature. The maxon and roton maxima were not found in the spectra; this is probably due to boundary effects. The droplet boundary is too close to the localized excitations, which are disturbed and thus quickly decay.

In the third system, the electronic and bosonic density functional methods were combined to study excess electrons in superfluid helium. The three first states of the one-electron bubbles were calculated. Each of the states has a unique shape which results from the delicate balance between the excess electron and helium. The properties obtained were compared to the classical bubble model, which was found to provide reasonably accurate results when a proper value is used for the classical surfaces tension. The singlet two-electron bubble was found to be stable in a spherical geometry; however, it was unstable against a small non-spherical perturbation. The triplet state was even more unstable as no stable geometries were found and the bubble dissociated without any perturbations. It was concluded that the two-electron bubbles appear to be unstable in superfluid ^{4}He.

Appendix A

Further information

A.1 The local spin-density approximation

The energy functional for the local spin-density approximation:

$$E_{xc}^{LSDA}[\rho_\alpha, \rho_\beta] = \int \rho(\vec{r})\varepsilon_{xc}^{LSDA}(\rho(\vec{r}), \zeta(\vec{r}))\, d^3r, \tag{A.1}$$

where $\rho(\vec{r}) = \rho_\alpha(\vec{r}) + \rho_\beta(\vec{r})$ is the total density, $\zeta(\vec{r}) = (\rho_\alpha(\vec{r}) - \rho_\beta(\vec{r}))/\rho(\vec{r})$ is the spin polarization parameter, and $\varepsilon_{xc}^{LSDA}(\rho(\vec{r}), \zeta(\vec{r}))$ is the energy per particle.

The exchange–correlation potential is obtained by taking the functional derivative with respect to spin-densities:

$$v_{xc,\alpha}^{LSDA}(\rho, \zeta) = \frac{\delta E_{xc}^{LSDA}}{\delta \rho_\alpha} = \varepsilon_{xc}(\rho, \zeta) + \rho\frac{\partial \varepsilon_{xc}}{\partial \rho} + (1 - \zeta)\frac{\partial \varepsilon_{xc}}{\partial \zeta} \tag{A.2}$$

and

$$v_{xc,\beta}^{LSDA}(\rho, \zeta) = \frac{\delta E_{xc}^{LSDA}}{\delta \rho_\beta} = \varepsilon_{xc}(\rho, \zeta) + \rho\frac{\partial \varepsilon_{xc}}{\partial \rho} - (1 + \zeta)\frac{\partial \varepsilon_{xc}}{\partial \zeta}\,. \tag{A.3}$$

The exchange and correlation parts can be evaluated separately:

$$\varepsilon_{xc}(\rho, \zeta) = \varepsilon_x(\rho, \zeta) + \varepsilon_c(\rho, \zeta)\,. \tag{A.4}$$

A.1.1 Exchange

The exchange energy per particle is

$$\varepsilon_x(\rho,\zeta) = \varepsilon_x(\rho,0)\frac{\left[(1+\zeta)^{4/3} + (1-\zeta)^{4/3}\right]}{2} \tag{A.5}$$

where

$$\varepsilon_x(\rho,0) = -C_x\rho^{1/3}\,, \tag{A.6}$$

and $C_x = \frac{3}{4}\left(\frac{3}{\pi}\right)^{1/3}$.

A.1.2 Correlation

The correlation energy per particle is

$$\varepsilon_c(\rho,\zeta) = \varepsilon_c^0(\rho) + \alpha(\rho)\left[\frac{f(\zeta)}{f''(0)}\right](1-\zeta^4) + (\varepsilon_c^1(\rho) - \varepsilon_c^0(\rho)f(\zeta)\zeta^4\,, \tag{A.7}$$

where

$$\varepsilon^0_(\rho) = q(x; A^0, x_0^0, b^0, c^0)\,, \tag{A.8}$$

$$\varepsilon^1_(\rho) = q(x; A^1, x_0^1, b^1, c^1)\,, \tag{A.9}$$

$$\alpha(\rho) = q(x; A^\alpha, x_0^\alpha, b^\alpha, c^\alpha)\,, \tag{A.10}$$

$$f(\zeta) = \frac{1}{2(2^{1/3}-1)}\left((1+\zeta)^{4/3} + (1-\zeta)^{4/3} - 2\right)\,, \tag{A.11}$$

$$\begin{aligned} q(x; A, x_0, b, c) = A\Bigg\{ &\ln\frac{x^2}{X(x)} + \frac{2b}{Q}\arctan\frac{Q}{2x+b} \\ &- \frac{bx_0}{X(x_0)}\Bigg[\ln\frac{(x-x_0)^2}{X(x)} \\ &+ \frac{2(b+2x_0)}{Q}\arctan\frac{Q}{2x+b}\Bigg]\Bigg\}\,, \end{aligned} \tag{A.12}$$

$x = \left(\frac{3}{4\pi\rho}\right)^{1/6}$, $X(x) = x^2 + bx + c$ and $Q = (4c - b^2)^{1/2}$.

	A	x_0	b	c
ε_c^0	0.03109070	-0.10498	3.72744	12.9352
ε_c^1	0.01554535	-0.32500	7.06042	18.0578
α	-0.01688686	-0.0047584	1.13107	13.0045

Table A.1: Values of parameters A, x_0, b, and c in atomic units.

The derivative of the function $q(x; A, x_0, b, c)$ with respect to x has a simple form:

$$\frac{\partial q(x; A, x_0, b, c)}{\partial x} = 2A \frac{c(x - x_0) - b x x_0}{x(x - x_0)X(x)} \,. \tag{A.13}$$

A.2 Alternative derivation of diffusion Monte Carlo

We start with time-dependent Schödinger equation:

$$i\hbar\frac{\partial\psi(\vec{r},t)}{\partial t} = -\frac{\hbar^2}{2m}\nabla^2\psi(\vec{r},t) + V[\psi(\vec{r},t)]\psi(\vec{r},t)\,. \tag{A.14}$$

Multiply (A.14) by wavefunction $\phi(\vec{r},t)$, which is the ground state wavefunction of an auxiliary bosonic system, to obtain:

$$\begin{aligned} i\hbar\phi(\vec{r},t)\frac{\partial\psi(\vec{r},t)}{\partial t} \\ &= -\frac{\hbar^2}{2m}\phi(\vec{r},t)\nabla^2\psi(\vec{r},t) + \phi(\vec{r},t)V[\psi(\vec{r},t)]\psi(\vec{r},t)\,. \end{aligned} \tag{A.15}$$

Insert $E'\phi(\vec{r},t) = i\hbar\frac{\partial\phi(\vec{r},t)}{\partial t}$ multiplied by $\psi(\vec{r},t)$:

$$\begin{aligned} i\hbar\phi(\vec{r},t)\frac{\partial\psi(\vec{r},t)}{\partial t} + i\hbar\psi(\vec{r},t)\frac{\partial\phi(\vec{r},t)}{\partial t} \\ &= -\frac{\hbar^2}{2m}\phi(\vec{r},t)\nabla^2\psi(\vec{r},t) + \phi(\vec{r},t)V[\psi(\vec{r},t)]\psi(\vec{r},t) \\ &\qquad + E'\psi(\vec{r},t)\phi(\vec{r},t) \end{aligned} \tag{A.16}$$

and rewrite:

$$\begin{aligned} i\hbar\frac{\partial\phi(\vec{r},t)\psi(\vec{r},t)}{\partial t} \\ &= -\frac{\hbar^2}{2m}\nabla^2[\phi(\vec{r},t)\psi(\vec{r},t)] + 2\frac{\hbar^2}{2m}\nabla\cdot[\psi(\vec{r},t)\nabla\phi(\vec{r},t)] \\ &\quad - \frac{\hbar^2}{2m}\psi(\vec{r},t)\nabla^2\phi(\vec{r},t) + \phi(\vec{r},t)V[\psi(\vec{r},t)]\psi(\vec{r},t) \\ &\qquad + E'\psi(\vec{r},t)\phi(\vec{r},t)\,. \end{aligned} \tag{A.17}$$

Denote $f(\vec{r},t) = \phi(\vec{r},t)\psi(\vec{r},t)$ and rewrite again:

$$\begin{aligned} i\hbar\frac{\partial f(\vec{r},t)}{\partial t} &= -D\nabla^2 f(\vec{r},t) \\ &\quad + D\nabla\cdot[F_Q(\vec{r},t)f(\vec{r},t)] + (E_L(\vec{r},t) + E')f(\vec{r},t)\,, \end{aligned} \tag{A.18}$$

where $D = \frac{\hbar^2}{2m}$, $F_Q(\vec{r},t) = 2\frac{\nabla\phi(\vec{r},t)}{\phi(\vec{r},t)}$ and

$$E_L(\vec{r},t) = \frac{1}{\phi(\vec{r},t)}\left[-\frac{\hbar^2}{2m}\nabla^2\phi(\vec{r},t) + V[\psi(\vec{r},t)]\phi(\vec{r},t)\right]. \tag{A.19}$$

Replace the real-time t with the imaginary time $\tau = it/\hbar$:

$$\begin{aligned}\frac{\partial f(\vec{r},\tau)}{\partial\tau} &= D\nabla^2 f(\vec{r},\tau) \\ &\quad - D\nabla\cdot[F_Q(\vec{r},\tau)f(\vec{r},\tau)] - (E_L(\vec{r},\tau) + E')f(\vec{r},\tau).\end{aligned} \tag{A.20}$$

Finally, shift the energy by replacing E' by $E_T = -E'$:

$$\begin{aligned}\frac{\partial f(\vec{r},\tau)}{\partial\tau} &= D\nabla^2 f(\vec{r},\tau) \\ &\quad - D\nabla\cdot[F_Q(\vec{r},\tau)f(\vec{r},\tau)] - (E_L(\vec{r},\tau) - E_T)f(\vec{r},\tau).\end{aligned} \tag{A.21}$$

In the variational Monte Carlo $\phi(\vec{r},\tau) = \psi(\vec{r},\tau)$ and the potential $V[\psi(\vec{r},\tau)]$ is the potential of an auxiliary system, the ground state of which is $\phi(\vec{r},\tau)$. $E_L(\vec{r},\tau)$ is just a constant and can be set to $E_L = E_T$:

$$\frac{\partial f(\vec{r},\tau)}{\partial\tau} = D\nabla^2 f(\vec{r},\tau) - D\nabla\cdot[F_Q(\vec{r},\tau)f(\vec{r},\tau)], \tag{A.22}$$

where $f(\vec{r},\tau) = |\phi(\vec{r},\tau)|^2$.

A.3 Accuracy of semi-implicit propagators

Non-linear Schrödinger equation:

$$i\hbar\frac{\partial\psi(\vec{r},t)}{\partial t} = H[\psi(\vec{r},t)]\psi(\vec{r},t)\,. \tag{A.23}$$

A.3.1 Non-linear explicit Euler

$$i\hbar\frac{\psi(\vec{r},t+\Delta t)-\psi(\vec{r},t)}{\Delta t} + \mathcal{O}(\Delta t) = H[\psi(\vec{r},t)]\psi(\vec{r},t) \tag{A.24}$$

$$\psi(\vec{r},t+\Delta t) = \left(1-\frac{i}{\hbar}H[\psi(\vec{r},t)]\Delta t\right)\psi(\vec{r},t) + \mathcal{O}(\Delta t^2)\,. \tag{A.25}$$

A.3.2 Non-linear semi-implicit Euler

Predictor step:

$$i\hbar\frac{\psi(\vec{r},t)-\psi(\vec{r},t-\Delta t)}{\Delta t} + \mathcal{O}(\Delta t) = H[\psi(\vec{r},t)]\psi(\vec{r},t)\,. \tag{A.26}$$

Substitute $H[\psi(\vec{r},t)] = H[\psi(\vec{r},t-\Delta t)+\mathcal{O}(\Delta t)]$:

$$i\hbar\frac{\psi(\vec{r},t)-\psi(\vec{r},t-\Delta t)}{\Delta t} + \mathcal{O}(\Delta t) = H[\psi(\vec{r},t-\Delta t)+\mathcal{O}(\Delta t)]\psi(\vec{r},t)\,. \tag{A.27}$$

If

$$H[\psi(\vec{r},t-\Delta t)+\mathcal{O}(\Delta t)] = H[\psi(\vec{r},t-\Delta t)] + \mathcal{O}(\Delta t^{\alpha}) \tag{A.28}$$

where $\alpha \geq 1$, then:

$$\left(1+\frac{i}{\hbar}H[\psi(\vec{r},t-\Delta t)]\Delta t\right)\tilde{\psi}(\vec{r},t) = \psi(\vec{r},t-\Delta t) + \mathcal{O}(\Delta t^2)\,. \tag{A.29}$$

Corrector step:

$$i\hbar\frac{\psi(\vec{r},t)-\psi(\vec{r},t-\Delta t)}{\Delta t} + \mathcal{O}(\Delta t) = H[\tilde{\psi}(\vec{r},t)+\mathcal{O}(\Delta t^2)]\psi(\vec{r},t) \tag{A.30}$$

$$\left(1+\frac{i}{\hbar}H[\tilde{\psi}(\vec{r},t)]\Delta t\right)\psi(\vec{r},t) = \psi(\vec{r},t-\Delta t) + \mathcal{O}(\Delta t^2)\,. \tag{A.31}$$

A.3.3 Non-linear semi-implicit Crank-Nicolson

Predictor step:

$$i\hbar\frac{\psi(\vec{r},t+\Delta t/2)-\psi(\vec{r},t-\Delta t/2)}{\Delta t}+\mathcal{O}(\Delta t^2)=H[\psi(\vec{r},t)]\psi(\vec{r},t)\,. \tag{A.32}$$

Substitute $H[\psi(\vec{r},t)] = H[\psi(\vec{r},t-\Delta t/2)+\mathcal{O}(\Delta t)]$
and $\psi(\vec{r},t)=\frac{1}{2}\left(\psi(\vec{r},t+\Delta t/2)+\psi(\vec{r},t-\Delta t/2)+\mathcal{O}(\Delta t^2)\right)$:

$$\begin{aligned}i\hbar&\frac{\psi(\vec{r},t+\Delta t/2)-\psi(\vec{r},t-\Delta t/2)}{\Delta t}+\mathcal{O}(\Delta t^2)\\&=H[\psi(\vec{r},t-\Delta t/2)+\mathcal{O}(\Delta t)]\times\\&\quad\frac{1}{2}\left(\psi(\vec{r},t+\Delta t/2)+\psi(\vec{r},t-\Delta t/2)+\mathcal{O}(\Delta t^2)\right)\,.\end{aligned} \tag{A.33}$$

If

$$H[\psi(\vec{r},t-\Delta t/2)+\mathcal{O}(\Delta t)]=H[\psi(\vec{r},t-\Delta t/2)]+\mathcal{O}(\Delta t^{\alpha}) \tag{A.34}$$

where $\alpha \geq 1$, then:

$$\begin{aligned}&\left(1+\frac{1}{2}\frac{i}{\hbar}H[\psi(\vec{r},t-\Delta t/2)]\Delta t\right)\tilde{\psi}(\vec{r},t+\Delta t/2)\\&\quad=\left(1-\frac{1}{2}\frac{i}{\hbar}H[\psi(\vec{r},t-\Delta t/2)]\Delta t\right)\psi(\vec{r},t-\Delta t/2)+\mathcal{O}(\Delta t^2)\,.\end{aligned} \tag{A.35}$$

Corrector step:

Because

$$H[\psi(\vec{r},t-\Delta t/2)]=H[\psi(\vec{r},t)]-\frac{\Delta t}{2}\frac{\delta H[\psi(\vec{r},t)]}{\delta\psi(\vec{r},t)}\frac{\partial\psi(t)}{\partial t}+\mathcal{O}(\Delta t^2) \tag{A.36}$$

and

$$H[\psi(\vec{r},t+\Delta t/2)]=H[\psi(\vec{r},t)]+\frac{\Delta t}{2}\frac{\delta H[\psi(\vec{r},t)]}{\delta\psi(\vec{r},t)}\frac{\partial\psi(t)}{\partial t}+\mathcal{O}(\Delta t^2) \tag{A.37}$$

thus

$$\tilde{H}(t)=\frac{1}{2}\left(H[\psi(\vec{r},t+\Delta t/2)]+H[\psi(\vec{r},t-\Delta t/2)]\right)+\mathcal{O}(\Delta t^2) \tag{A.38}$$

If

$$H[\psi(\vec{r},t+\Delta t/2)+\mathcal{O}(\Delta t^2)] = H[\psi(\vec{r},t+\Delta t/2)] + \mathcal{O}(\Delta t^\alpha) \tag{A.39}$$

where $\alpha \geq 2$, then:

$$\begin{aligned}\left(1+\frac{1}{2}\frac{i}{\hbar}\tilde{H}(t)\Delta t\right)\psi(\vec{r},t+\Delta t/2)\\ = \left(1-\frac{1}{2}\frac{i}{\hbar}\tilde{H}(t)\Delta t\right)\psi(\vec{r},t-\Delta t/2)+\mathcal{O}(\Delta t^3)\end{aligned} \tag{A.40}$$

A.3.4 Example: Gross–Pitaevskii potential

Because

$$V[\psi(\vec{r},t)] = g|\psi(\vec{r},t)|^2 \tag{A.41}$$

thus

$$\begin{aligned}V[\psi(\vec{r},t)+\delta\psi(\vec{r})\mathcal{O}(\Delta t^\alpha)] &= g|\psi(\vec{r},t)+\delta\psi(\vec{r})\mathcal{O}(\Delta^\alpha)|^2\\ &= g|\psi(\vec{r},t)|^2 + g\left(\psi(\vec{r},t)\delta\psi^*(\vec{r})+\psi^*(\vec{r},t)\delta\psi(\vec{r})\right)\mathcal{O}(\Delta t^\alpha)\\ &\quad + g|\delta\psi(\vec{r})|^2\mathcal{O}(\Delta t^{2\alpha})\\ &= g|\psi(\vec{r},t)|^2+\mathcal{O}(\Delta t^\alpha)\,.\end{aligned} \tag{A.42}$$

Bibliography

[1] P. Kapitza, Nature **141**, 74 (1938), reference taken from [2].

[2] I. M. Khalatnikov, in *The physics of liquid and solid helium*, edited by K. H. Bennemann and J. B. Ketterson (A Wiley-Interscience Publication, New York, 1976).

[3] L. D. Landau, Journal of Experimental and Theoretical Physics **11**, 592 (1941).

[4] R. P. Feynman, Physical Review **91**, 1291 (1953).

[5] R. P. Feynman, Physical Review **91**, 1301 (1953).

[6] R. P. Feynman, Physical Review **94**, 262 (1954).

[7] R. P. Feynman, Physical Review **102**, 1189 (1956).

[8] R. P. Feynman, in *Progress in Low Temperature Physics, Vol. I, 2nd ed.*, edited by J. C. Gorter (North-Holland Publishing Company, Amsterdam, 1957), pp. 17–53.

[9] *Atomic energy levels*, edited by C. E. Moore (National bureau of standars, Washington DC, 1971).

[10] F. Luo *et al.*, Journal of Chemical Physics **98**, 3564 (1993).

[11] A. R. Janzen and R. A. Aziz, Journal of Chemical Physics **107**, 914 (1997).

[12] B. Liu and A. D. McLean, Journal of Chemical Physics **91**, 2348 (1989).

[13] *Superfluidity and superconductivity*, edited by D. R. Tilley and J. Tilley (John Wiley & Sons, New York, 1974).

[14] L. Tisza, Physical Review **72**, 838 (1947).

[15] F. London, Physical Review **54**, 947 (1938).

[16] R. A. Cowley and A. D. B. Woods, Canadian Journal of Physics **49**, 177 (1971).

[17] A. F. V. J. Peter Toennies, Annual Review of Physical Chemistry **49**, 1 (1998).

[18] A. Trottier, A. I. Jirasek, H. F. Tiedje, and R. L. Brooks, Physical review A **61**, 052504 (2000).

[19] S. Grebenev *et al.*, Physica B **280**, 65 (2000).

[20] F. Stienkemeier and A. F. Vilesov, Journal of Chemical Physics **115**, 10119 (2001).

[21] Y. Kwon *et al.*, Journal of Chemical Physics **113**, 6469 (2000).

[22] G. Ihas and T. M. Sanders, Jr., Physical Review Letters **27**, 1383 (1971).

[23] A. Ghosh and H. J. Maris, Physical Review Letters **95**, 265301 (2005).

[24] J. Levine and T. M. Sanders, Jr., Physical Review Letters **8**, 159 (1962).

[25] L. Thomas, Proceeding of the Cambridge Philosophical Society **23**, 542 (1927).

[26] E. Fermi, Atti della Accademia Nazionale dei Lincei, Rendiconti, Classe di Scienze Fisiche, Matematiche e Naturali **6**, 602 (1927).

[27] E. Fermi, Zeit für Physik **48**, 73 (1928).

[28] P. Hohenberg and W.Kohn, Physical Review **126**, B864 (1964).

[29] M. Levy, Physical Review A **26**, 1200 (1982).

[30] E. Runge and E. K. U. Gross, Physical Review Letters **52**, 997 (1984).

[31] H. Kohl and R. M. Dreizler, Physical Review Letters **56**, 1993 (1986).

[32] M. A. L. Marques and E. K. U. Gross, in *A primer in density functional theory*, edited by C. Fiolhais, F. Nogueira, and M. Marques (Spinger-Verlag, Berlin, 2003), pp. 144–184.

[33] W. Kohn and L. J. Sham, Physical Review **140**, A1133 (1965).

[34] J. P. Perdew and S. Kurth, in *A primer in density functional theory*, edited by C. Fiolhais, F. Nogueira, and M. Marques (Spinger-Verlag, Berlin, 2003), pp. 1–55.

[35] S. H. Vosko, L. Wilk, and M. Nusair, Canadian Journal of Physics **58**, 1200 (1980).

[36] D. M. Ceperley and B. J. Adler, Physical Review Letters **45**, 566 (1980).

[37] J. P. Perdew and A. Zunger, Physical Review B **23**, 5048 (1981).

[38] J. P. Perdew, A. Savin, and K. Burke, Physical Review A **51**, 4531 (1995).

[39] E. P. Gross, Nuovo Cimento **20**, 454 (1961).

[40] E. P. Gross, Journal of Mathematical Physics **4**, 195 (1963).

[41] L. P. Pitaevskii, Journal of Experimental and Theoretical Physics **13**, 451 (1961).

[42] A. L. Fetter, in *The physics of liquid and solid helium*, edited by K. H. Bennemann and J. B. Ketterson (A Wiley-Interscience Publication, New York, 1976).

[43] S. Stringari and J. Treiner, Journal of Chemical Physics **87**, 5021 (1987).

[44] J. Dupont-Roc, M. Himbert, N. Pavioff, and J. Treiner, Journal of Low Temperature Physics **81**, 31 (1990).

[45] N. Berloff, Journal of Low Temperature Physics **116**, 359 (1999).

[46] F. Dalfovo *et al.*, Physical Review B **52**, 1193 (1995).

[47] B. L. Hammond, W. A. Lester, Jr., and P. J. Reynols, *Monte Carlo methods in ab initio quantum chemistry* (World Scientific, Singapore, 1994).

[48] J. Toivanen, private communication.

[49] M. Frigo and S. G. Johnson, ICASSP Conference Proceedings 3 **3**, 1381 (1998), for more details see http://www.fftw.org.

[50] *OpenMP C and C++ Application Program Interface, Version 1.0*, OpenMP Architecture Review Board, 1998, for more details see http://www.openmp.org.

[51] M. Aichinger and E. Krotscheck, Computational Material Science **34**, 6841 (2005).

[52] S. A. Chin, Physical Letters A **226**, 344 (1997).

[53] G. H. Golub and C. F. Van Loan, *Matrix Computations* (North Oxford Academic, Oxford, 1983).

[54] J. Jortner, L. Meyer, S. A. Rice, and E. G. Wilson, Physical Review Letters **12**, 415 (1964).

[55] J. W. Keto, F. J. Soley, M. Stockton, and W. A. Fitzsimmons, Physical Review A **10**, 887 (1974).

[56] A. V. Benderskii, R. Zadoyan, N. Schwentner, and V. A. Apkarian, Journal of Chemical Physics **110**, 1542 (1999).

[57] J. L. Persson, Q. Hui, M. Nakamura, and M. Takami, Physical Review A **52**, 2011 (1995).

[58] R. Lehoucq and J. A. Scott, *An evaluation of software for computing eigenvalues of sparse nonsymmetric matrices*, 1996, preprint MCS-P547-1195, Argonne National Laboratory, see http://www.caam.rice.edu/software/ARPACK/ for more details.

[59] P. W. Anderson, Physical Review **86**, 809 (1952).

[60] S. Bloom and H. Margenau, Physical Review **90**, 791 (1953).

[61] J. Eloranta, H. Y. Seferyan, and V. A. Apkarian, Chemical Physics Letters **396**, 155 (2004).

[62] M. Hartmann, F. Mielke, J. P. Toennies, and A. F. Vilesov, Physical Review Letters **76**, 4560 (1996).

[63] P. Sindzingre, M. L. Klein, and D. M. Ceperlay, Physical Review Letters **63**, 1601 (1989).

[64] W. B. Fowler and D. L. Dexter, Physical Review **176**, 337 (1968).

[65] C. C. Grimes and G. Adams, Physical Review B **41**, 6366 (1990).

[66] A. Y. Parshin and S. V. Pereverzev, Journal of Experimental and Theoretical Physics Letters **52**, 282 (1990).

[67] J. Classen, C.-K. Su, M. Mohazzab, and H. J. Maris, Physical Review B **57**, 3000 (1997).

[68] H. J. Maris, Journal of Low Temperature Physics **132**, 77 (2003).

[69] J. Eloranta and A. Apkarian, Journal of Chemical Physics **117**, 10139 (2002).

[70] H. J. Maris, Journal of Low Temperature Physics **120**, 173 (2000).

[71] H. J. Maris, A. Ghosh, D. Konstantinov, and M. Hirsch, Journal of Low Temperature Physics **134**, 227 (2004).

[72] J. Jortner, N. R. Kestner, S. A. Rice, and M. H. Cohen, Journal of Chemical Physics **43**, 2614 (1965).

[73] A. Ghosh and H. J. Maris, Physical Review B **72**, 054512 (2005).

PAPER I

https://doi.org/10.1103/PhysRevA.69.012506

"Solvation of triplet Rydberg states of molecular hydrogen in superfluid helium"
Toni Kiljunen, Lauri Lehtovaara, Henrik Kunttu, and Jussi Eloranta
Physical Review A, **69**, 012506 (2004)

PAPER II

https://doi.org/10.1016/j.jcp.2003.08.020

“Efficient numerical method for simulating static and dynamic properties of superfluid helium”
Lauri Lehtovaara, Toni Kiljunen, and Jussi Eloranta
Journal of Computational Physics, **194**, 78–91 (2004)

PAPER III

https://doi.org/10.1007/s10909-005-1533-7

“A 2-level anisotropic electronic system in superfluid ^{4}He”
Lauri Lehtovaara and Jussi Eloranta
Journal of Low Temperature Physics, **138**, 91–96 (2005)

PAPER IV

https://doi.org/10.1016/j.jcp.2006.06.006

“Solution of time-independent Schrödinger equation by the imaginary time propagation method”
Lauri Lehtovaara, Jari Toivanen, and Jussi Eloranta
Journal of Computational Physics, **221**, 128–157 (2007)

PAPER V

https://doi.org/10.1007/s10909-007-9348-3

"One and two-electron bubbles in superfluid ^{4}He"
Lauri Lehtovaara and Jussi Eloranta
Journal of Low Temperature Physics, in press (2007)